

Effect of quartz on antigorite gouges: friction decrease by talc formation or pressure solution.

L. ten Thij (6359426)

HPT laboratory, Department of Earth Sciences
Utrecht University, The Netherlands
Master thesis under supervision of Dr. A.R. Niemeijer

May 5, 2021

1 Abstract

Normally conditions in the forearc mantle wedge would cause stick-slip behaviour. However, the forearc mantle wedge shows aseismic behaviour. Sections of the San Andreas fault also show aseismic behaviour. Previous work suggested that serpentine was the cause of this aseismic behaviour, in both forearc mantle wedges and the San Andreas fault. However, serpentine normally experiences temperature strengthening and causes stick-slip in laboratory experiments, which means that other weakening mechanisms are causing the aseismic behaviour. D E Moore et al., 2013 showed that when serpentine is sheared against quartz it experiences decreasing friction with increasing temperature. One explanation for this decrease could be the formation of talc due to its low friction in comparison to serpentine. A reaction of serpentine with silica rich sources will form talc which is stable over a wide range of temperature–pressure conditions and has a very low friction coefficient. A second explanation is the activation of pressure solution which is activated by the presence of quartz. Up till now, research on this topic has only been done up to temperatures of 350°C and few experiments have been conducted with quartz incorporated in the antigorite gouge. In this research I show the effect of different weight percentages of quartz on the friction of antigorite at temperatures up to 500°C. Experiments were conducted with the rotary shear apparatus at different velocities. The experiments may give an insight in the frictional strength, expressed using the rate and state parameters (a-b). Microstructural data of the experiments can give an insight in the active deformation mechanisms in antigorite mixed with quartz during shearing. Experiments conducted with antigorite containing quartz, show a significant decrease in friction and positive (a-b) values which suggests that shearing is aseismic. Results from the microprobe, EDX and FTIR prove the formation of talc during the experiments at temperatures of 500°C and the presence of pressure-solution by pressure shadows and the dependence on grain size. In nature, these two processes could be the cause of the aseismic behaviour within forearc mantle wedges and the San Andreas fault.

2 Introduction

Based on laboratory and field data (R. D. Hyndman et al., 1993), forearc mantle wedges appear to be aseismic even though the maximum temperature for earthquake behaviour in continental crustal compositions is about 350°C and pressures of 100 MPa to 2GPa, which corresponds to the onset of plasticity of quartz and encompasses most forearc mantle wedges. The brittle-ductile transition for dry mantle rocks, of which the rheology is controlled by olivine, at 600-800°C (Kirby, 1983) can not explain this aseismic behaviour because this exceeds the maximum temperature of most forearc upper mantles. If the forearc mantle wedge is made up out of dry mantle rocks, the forearc should be much stronger than crustal rocks (Kirby, 1983). This means that earthquakes might be expected to occur to considerable depth in forearc mantle. However, few if any earthquakes are found within the forearc mantle wedge.

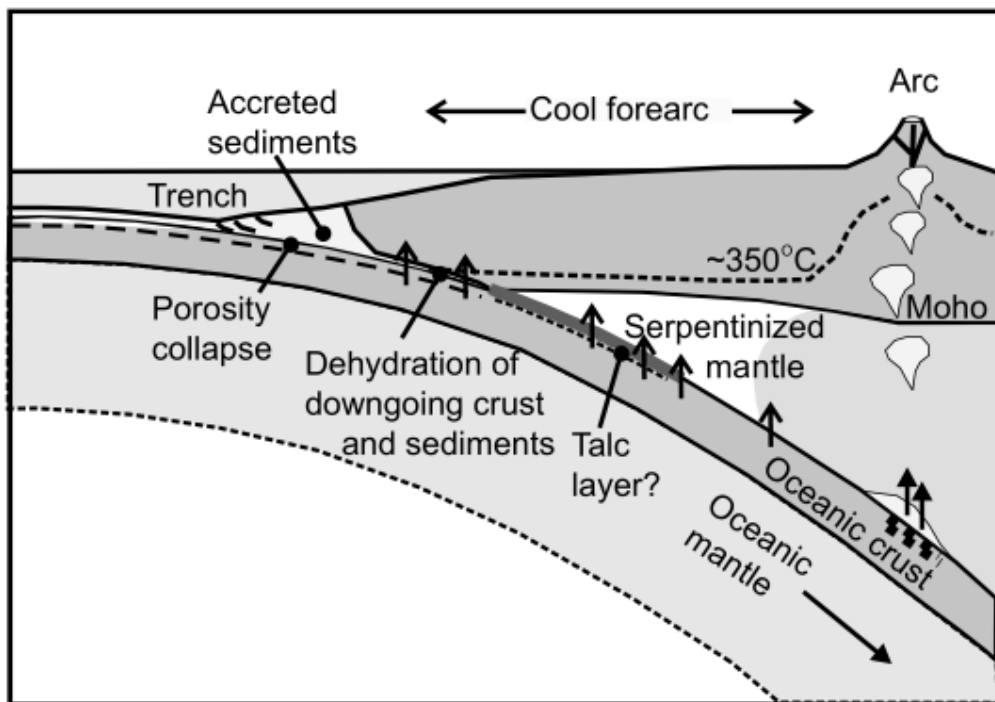
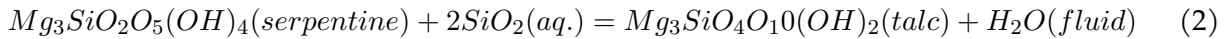
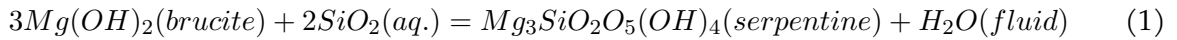


Figure 1: Schematic cross section illustrating fluid expulsion from subducting oceanic crust and sediments, and serpentinization of the overlying forearc mantle by D. Hyndman et al., 2003.

This aseismic behaviour of forearc mantle wedges has been suggested to be caused by serpentine. Hydrated minerals such as serpentine, talc and chlorite, form by fluids released from the subducting slab during metamorphic dehydration (D. Hyndman et al., 2003). The formation of hydrated minerals in the forearc mantle wedge begins at the base where fluids enter the forearc mantle wedge but, with sufficient and lasting fluid supply from the slab, the entire stagnant portion may be composed of hydrated minerals, especially at its tip (Reynard, 2013), see serpentinized mantle in figure 1. Solid-state mantle wedge flow directly above the weakened interface will thus be slow or absent. Stagnation of the mantle wedge in turn maintains cool and wet conditions to facilitate the formation of hydrated minerals, maintaining or enhancing interface decoupling (Padrón-Navarta et al., 2013, Angiboust et al., 2012, Hilairet et al., 2009).

In the forearc mantle wedge, talc may be formed along the plate interface where infiltrating silica-saturated fluids, derived from the underlying subducting crust, (Manning, 1996) and mechanical mixing of mantle with siliceous sediments may occur (Bebout et al., 1989). This infiltration of silica rich material is supported by seismic, laboratory and field evidence (Audet et al., 2014). At temperatures below 550°C, initial hydration of the mantle wedge produces serpentine and brucite. Over time, the continued migration of Si-charged fluids into the serpentinized ultramafic rocks first causes the conversion of any brucite present to serpentine, followed by the replacement of serpentine minerals by talc (Manning, 1995). Equation 1 and 2 show the formation pathway of serpentine and talc from brucite as written by S M Peacock et al., 1999. This reaction is a metasomatic process because it proceeds to the right if the silica content of the fluid increases and/ or if the water activity is lowered (Bach et al., 2004, Boschi et al., 2006).



Another system that has been proposed to be weakened by the presence of serpentine is a continental transform fault in western North America, the San Andreas fault (D E Moore et al., 1997; D E Moore et al., 2013). In central and northern California creeping behaviour is characterized by aseismic slip and microearthquakes. Serpentine within the San Andreas fault is found as serpentinite bodies. These serpentine bodies have been suggested to migrate to shallower depths due to their relative low density compared to the overlying rock column, a fault intersecting such a rock unit provides a pathway for the migration of serpentinite to shallower depths (E. Moore et al., 2007).

In the San Andreas fault talc is formed by a reaction of antigorite with dissolved silica content of heated ground water and from metastably deposited quartz veins, possibly resulting from focused fluid flow within the fault zone. The formation of talc in continental transform faults is identical to equation 2.

However, The reason of this aseismic behaviour within subduction zones and the San Andreas fault needs to be revisited, because serpentine at elevated temperatures is not weak and according to laboratory studies serpentine can even show frictionally unstable behaviour and cause stick-slip. Serpentine normally experiences an increase in friction coefficient with increasing temperature (temperature strengthening). However, D E Moore et al. showed that when sheared against quartzite at 350°C, strength can be reduced from 0.5-0.85 to values as low as 0.3. One explanation for this decrease in friction, when in contact with quartz, is the formation of talc (D E Moore et al., 2013).

Talc is stable over a wide range of temperature–pressure conditions ranging from surficial environments to the coesite-eclogite facies. The maximum stable depth for talc in the mantle wedge above the subducting slab or in subducted oceanic lithosphere will vary with its temperature profile.

The frictional properties of talc can be as low as 0.11 (D E Moore et al., 2008), and is related to relatively weak interlayer bonds and the preferred orientation of the platy grains. Talc can decrease the friction of the forearc mantle and San Andreas fault and could explain the aseismic behaviour if enough talc is produced.

A second explanation for the aseismic behaviour of both the forearc mantle wedge and the San Andreas fault is by pressure solution. Pressure solution is a deformation mechanism active at relatively low temperatures with the presence of an aqueous fluid. Materials at high stress boundaries dissolve, and then precipitate at a place of lower stress. D E Moore et al. showed that solution-transfer processes are promoted by the enhanced solubility of serpentine in pore fluids whose chemistry has been modified by the interaction of quartz. In the absence of geometric or other impediments, any active crustal fault that shears serpentine against quartzofeldspathic rocks has the potential for aseismic slip (creep) at the temperatures associated with seismogenic depths. Which means that if serpentine, within forearc mantle wedges or the San Andreas fault, comes in contact with a siliceous fluid, pressure solution may be active and cause the aseismic behaviour that is happening.

Most experiments performed up to now, to explain the aseismic behaviour of the forearc mantle wedge and the San Andreas fault, were performed at temperatures below 350°C and low shear strain (D E Moore et al., 1997; D E Moore et al., 2013; Okazaki et al., 2013). More experiments should be conducted at temperatures above 350°C, high shear strain and low velocities to get an insight in the friction development of antigorite at these temperatures when mixed with quartz. Furthermore, microstructural data is needed of the experiments to show if talc was formed or if other weakening mechanisms are active. If talc has formed did enough talc form to significantly decrease the friction of antigorite to cause the aseismic behaviour, this means that during our experiments a temperature drop should not increase friction. In our research i address how mixing of serpentine with subducted sediments or interaction with a silica-rich fluid might affect its frictional behaviour at temperatures up to 500°C and high shear strain.

2.1 Serpentine

Serpentine is not just one single mineral but consists of a group of hydrous magnesium-rich silicate minerals with an approximate composition of $Mg_3Si_2O_5(OH)_4$. It forms as a replacement mineral for olivine and pyroxenes in ultramafic igneous rocks at temperatures below 500-600°C in the presence of water (Evans et al., 1976). When fully serpentinized the mineral contains approximately 13% water by weight.

Serpentine has three polymorphs: lizardite, chrysotile and antigorite. All with a general composition of octahedral layers rich in $Mg[MgO_2(OH)_4]^{6-}$, attached to a tetrahedral silicate $[Si_2O_5]^{2-}$ sheet. Perpendicular to the sheet, tetrahedral-octahedral (T-O) layers are linked to other T-O layers by a weak H-bonding. The charge counterbalance can lead to a misfit between the T layers and O sheets, producing layers that are either curved or flat, which generates the three different polymorphs. This research will focus on antigorite.

Antigorite has slightly curved layers where the octahedral sheet is continuous, whereas the tetrahedral sheet undergoes periodic alterations, leading to some cross-connections with adjacent octahedral sheets through covalent Si-O bonds, as shown in figure 2. Due to this wavelike structure and the variability in length of these curved layers, some variations in composition and structure are common. Just like talc and other sheet-structure minerals the frictional properties are tied to the relatively weak interlayer bonds and the preferred orientation of the platy grains (D E Moore et al., 2008).

Antigorite is the high-temperature form of serpentine, being stable at temperatures from 200°C to 500-600°C and pressures of 5GPa at depths of up to 150-200km (D E Moore et al., 1997).

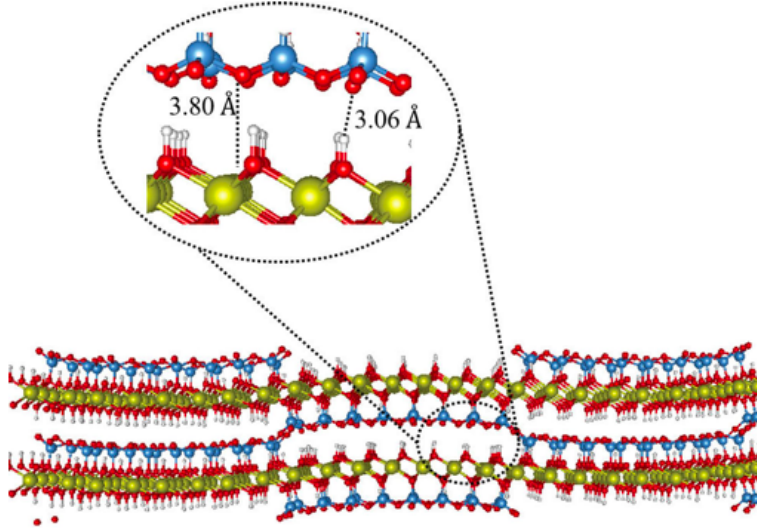


Figure 2: atomic structure of antigorite from Carmignano et al., 2020

2.2 Rate and state friction

In 1966 Brace et al. suggested stick–slip frictional instabilities in the lab might be equivalent to earthquakes. Thus, the earthquake is the ‘slip’, and the ‘stick’ is the interseismic period of elastic strain accumulation. Their work made two primary contributions to the modern Rate- and State-variable constitutive law in two ways. The first, involved the recognition of frictional stability as a system response determined by the frictional properties of the contacting surfaces and their elastic surroundings. The second contribution by Dieterich involved detailed measurements of the velocity dependence of sliding friction and the time dependence of static friction.

The first one led to a fundamental change in the way laboratory studies were carried out. Simple “mapping” studies of the stability boundary between stick-slip and stable sliding were recognized as having limited value, and they were gradually replaced by more detailed studies in which friction data were subject to sophisticated modeling in order to separate stability and friction properties from apparatus effects. This change in laboratory studies resulted in a way that friction data were increasingly cast in terms of constitutive parameters and constitutive laws that could be readily applied in a variety of mechanical settings, including those of seismogenic faults. The second one showed that static friction and dynamic friction are related which meant that a simple velocity dependent friction law, such as the slip weakening law, was not sufficient and that the existing friction laws were not adequate (Marone, 1998). The introduction of the Rate- and State-variable constitutive laws resolved this problem. These laws are given by equations 3 and 4 (sometimes known as the slowness law or ageing (Dieterich) law):

$$\mu = \mu_0 + a \ln \frac{V}{V_0} + b \ln \frac{V_0 \theta}{d_c} \quad (3)$$

$$\frac{d\theta}{dt} = 1 - \frac{V\theta}{d_c} \quad (4)$$

$$\mu_s = \frac{\tau}{\sigma_n} \quad (5)$$

Here, μ is the coefficient of friction, defined by equation 5, assuming that cohesion is zero, μ_0 is the coefficient of friction at a reference velocity V_0 , V is the instantaneous slip velocity, a is a parameter that quantifies the direct effect of friction, b is the parameter that describes the evolution effect of friction, d_c is a characteristic or critical slip displacement over which the state variable, θ , evolves. The state variable θ has units of time and is thought to represent the average lifetime of grain-scale asperity contacts. Due to the formulation in equation 3, also known as the ageing law, the frictional contact area continues to evolve in the absence of slip (Niemeijer et al., 2020).

The velocity dependence of friction can be obtained by rock friction experiments. In such an experiment, A simulated gouge or rock interface is sheared at a prescribed load-point velocity until steady state friction is reached (μ_{ss}). At this point, the velocity is instantaneously changed an order or half order magnitude (e.g., 0.01-0.03 $\mu\text{m/s}$) and the frictional response is recorded. This frictional response due to the instantaneous velocity change can be modeled using equation 3 and 4, coupled to an equation that describes the elastic interaction with the loading frame to obtain a , b and d_c (Niemeijer et al., 2020). At steady state, equations 3 and 4 reduce to the following equation:

$$(a - b) = \frac{d\mu_{ss}}{\ln\left(\frac{V_1}{V_0}\right)} \quad (6)$$

This equation can be used to calculate the value (a-b). The difference in a negative or positive (a-b) is the difference between potential earthquake nucleation or aseismic slip. When (a-b) is negative instabilities can nucleate which ultimately can lead to and stick-slip behaviour, depending on the elasticity of the system.

Three possible responses in friction can be seen at an up-step in velocity. Figure 3 shows those three responses. The upper one is velocity strengthening, when an upstep in velocity likewise increases the friction. The middle one shows velocity weakening, in this case increasing the velocity leads to a decrease in friction relative to the steady-state friction at the reference velocity. The lowest also shows velocity weakening though in a more compliant loading system, leading to the onset of oscillations. A further reduction in elasticity or a more negative (a-b) value would result in stick-slip behaviour.

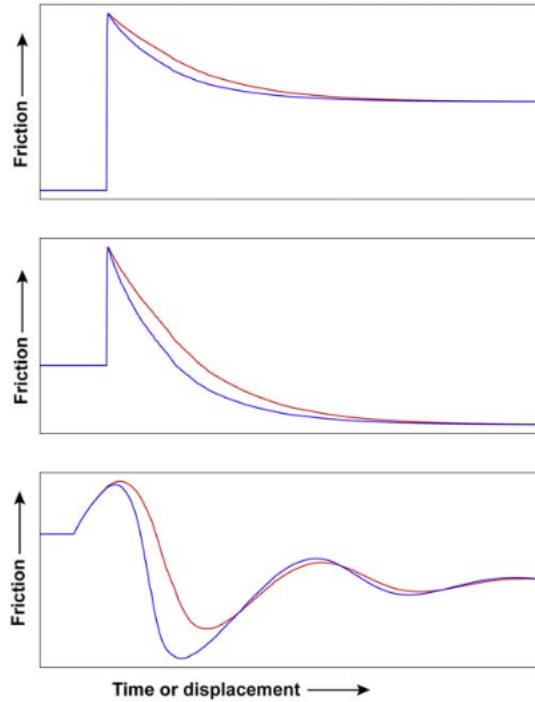


Figure 3: response of friction to an instantaneous up-step in load-point velocity. Niemeijer et al., 2020

2.3 Pressure solution

Deformation of rocks on the scale of individual grains can happen through a large number of processes. The exact processes involved depend on several factors such as mineralogy, composition of the intergranular fluid, grain size, etc; but also on external controls such as temperature, lithostatic pressure, differential stress, fluid pressure and externally imposed strain rate. One of those deformation processes is pressure solution (Passchier et al., 2005). Pressure solution is commonly encountered in rocks which have suffered diagenetic or low grade metamorphic grade conditions.

Pressure solution is localised where stress in the grain is high because the solubility of a mineral in an aqueous fluid is higher where a crystal lattice is under high stress than at localities where stress is relatively low (Passchier et al., 2005). The pressure solution process occurs in three stages. The first stage is dissolution at the grain contacts where stress is high. The Second stage is diffusion of the dissolved material to a site of low stress and lastly, the precipitation of the dissolved material at the site of low stress. An intergranular aqueous phase enhances the kinetics of the intergranular diffusion, so that the process can take place at an appreciable rate at relatively low temperatures, $0,3 \cdot T_m$ (melting point) of antigorite. In polymineralic rocks newly precipitated material may be of a different mineral composition or phase compared to the dissolved material. This process is known as incongruent pressure solution (Rutter, 1983). A general equation for the operation of pressure solution in simple shear is given as:

$$\dot{\gamma} \propto \tau^1 \exp\left(\frac{-\Delta H}{RT}\right) d^p \quad (7)$$

In this equation, taken from Bos et al., $\dot{\gamma}$ is the strain rate, τ is the shear stress, ΔH is the parameter which measures its temperature sensitivity, the heat of activation for flow (activation enthalpy). R is the gas constant and T is temperature in kelvin. When rewriting this equation $\ln\left(\frac{\dot{\gamma}}{\tau}\right)$ can be plotted against $\frac{1}{RT}$, the slope of this graph should be ΔH assuming that there are no complicating factors such as phase transformations, changes in the dominant deformation mechanism or porosity differences which changes the stress at the grain contacts. Pressure solution processes can be observed in the laboratory time scale at high temperatures, which might occur in nature at lower temperatures over a much larger time scale. This principle works well when ΔH is large (-200 kJ/mol or more), as is the case for intracrystalline plastic processes. If ΔH is small, however, a very large temperature increment would be required to produce a given rate change (Rutter, 1983). Other evidence for pressure solution are its microstructural phenomena that can be observed. Interesting for this research is the migration of "soluble" material from the sides of stressed object facing principal loading directions to the 'pressure shadow' areas.

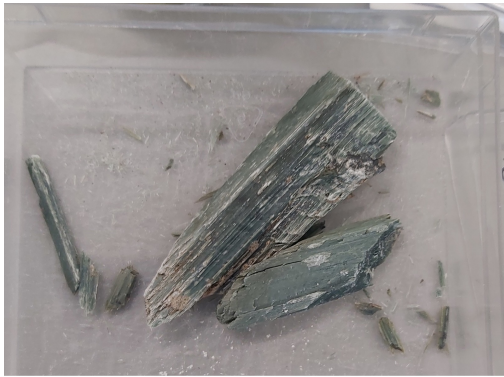


Figure 4: antigorite used during this research

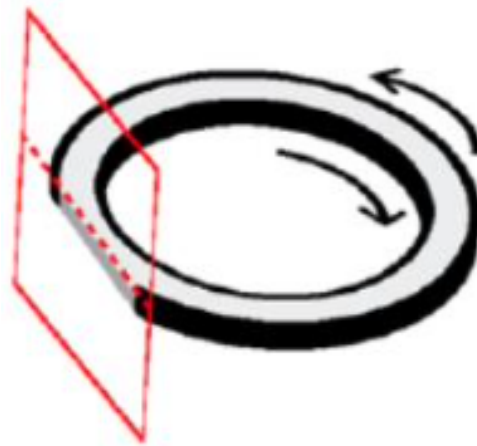


Figure 5: schematic presentation of the position used for making thin sections (Verberne et al., 2015).

3 Materials

The antigorite used in the experiments was sampled in Spain. It has a greenish colour and a layered structure, see figure 4. To get the composition of the antigorite, two analyses were done. These analyses were done on the sample from experiment u866 which was conducted at room temperature and therefore no reaction took place during the experiment as confirmed by Fourier transform infra-red (FTIR) analyses. Therefore this sample can be used for analyses of the starting material. Energy-dispersive x-ray (EDs) showed that a few grains of magnetite are present in the sample. The second analyses was the microprobe. These results gave the exact composition of the antigorite grains. Table 1 shows the composition of the oxides present in the antigorite. The values are averages calculated from 44 measurements done on the antigorite grains. Due to the presence of aluminium the origin of the sample is suggested to be serpentinization from pyroxene as opposed to olivine.

oxide	percentage	standard deviation
SiO ₂	43,07	0.6094
MgO	37,20	0.9722
FeO	4,27	0.1214
Al ₂ O ₃	1,46	0.0669
NiO	0,15	0.0530
MnO	0,10	0.0167
CaO	0,02	0.0080
H ₂ O	12,81	0.0354
total	99,09	

Table 1: composition of the antigorite. The standard deviation was calculated from 44 measurements one the sample.

The quartz used in all experiments is a commercial product known as min-u-sil 15 (US silica company). The grain size of this quartz is for at least 95% smaller than 5 μ m. It has a bright white colour and is for at least 99.2% SiO₂ (product data: silica ground n.d.).

4 Sample preparation and installation

The first step preparing the samples was crushing the antigorite. This was done by hand with a mortar and pestle. The crushed grains were separated using mesh sieves with diameters of 106, 45 and 25 μ m. Most experiments were conducted with antigorite that had a grain size between 45

to 106 μm . For the experiments where the start material contained quartz, 5 or 10 wt% quartz was added to antigorite to get the desired ratios, see table 2 for all experiments conducted.

For almost all experiments the antigorite or quartz-antigorite mixture is positioned in the pistons between the two confining rings as described in chapter 6. Solely for experiment u859 the quartz was not incorporated within the antigorite. The antigorite was positioned between the two confining rings and the quartz was positioned within the inner confining ring.

After the experiments the samples were prepared for analyses by drying the samples in a 50°C oven. Upon removal of the confining rings, the sample would crumble in smaller pieces. The bigger pieces were used to make thin sections from which the microstructures in the shear plane could be studied, see figure 5. The remaining sample was used for other analyses that will be described in section 5.2.

5 Methods

5.1 Rotary shear apparatus

All frictional sliding experiments were performed in a hydrothermal rotary shear apparatus as described by AR Niemeijer et al. (2008) and Den Hartog et al. (2012). Figure 6 shows the rotary shear apparatus, pressure vessel and the positioning of the sample between the two pistons. In this apparatus the sample material is positioned between roughened upper and lower pistons and is kept in place by two confining rings. The piston assembly is positioned in an internally heated, 300 MPa pressure vessel filled with distilled water, which serves as the pore fluid. Fluid pressure is applied to the water in the pressure vessel using a manually driven pump. Convection of the pore fluid is prevented by an insulating mullite tube. A teflon ring between the mullite tube and the piston head protects the piston head against corrosion. The outside wall of the vessel is sheathed in a water-cooling jacket, see figure 6b. The pressure vessel is closed with the upper closure nut and is positioned in a 100KN Instron loading frame, where the lower forcing block is coupled to the underlying servo-controlled motor and gearbox, which in turn is rigidly coupled to the vertical loading ram of the Instron used to apply the normal stress during the experiments. The required effective normal stress is applied to the gouge by axially loading the piston assembly, from the top, via a pressure-compensated piston. This means that the applied force on the outside is transferred completely to the sample, minus a small amount of force supported by the seals.

The electro-motor and gearbox rotate the vessel and lower piston and can produce shearing velocities of ~ 0.001 to $\sim 300 \mu\text{m/s}$ as measured on the average radius of the ring (12.5 mm). The upper piston is kept stationary by a bar on the upper forcing block which stops the rotation. The upper forcing block is equipped with two load cells which measure the torque applied to the system by the rotational movement which is then converted into shear stress. The normal stress is measured by an axial load cell. The temperature in the furnace coil, which can reach temperatures of up to 700°C, is measured with a thermocouple. One port in the upper sealing head provides access for the pore fluid system, two are cooling water conduits and a final port provides access for a thermocouple located close to the sample, see figure 6c.

To assemble the apparatus to start an experiment, approximately 0.5 gr gouge material is loaded between the two confining rings on the lower piston. The lower and upper internal pistons are

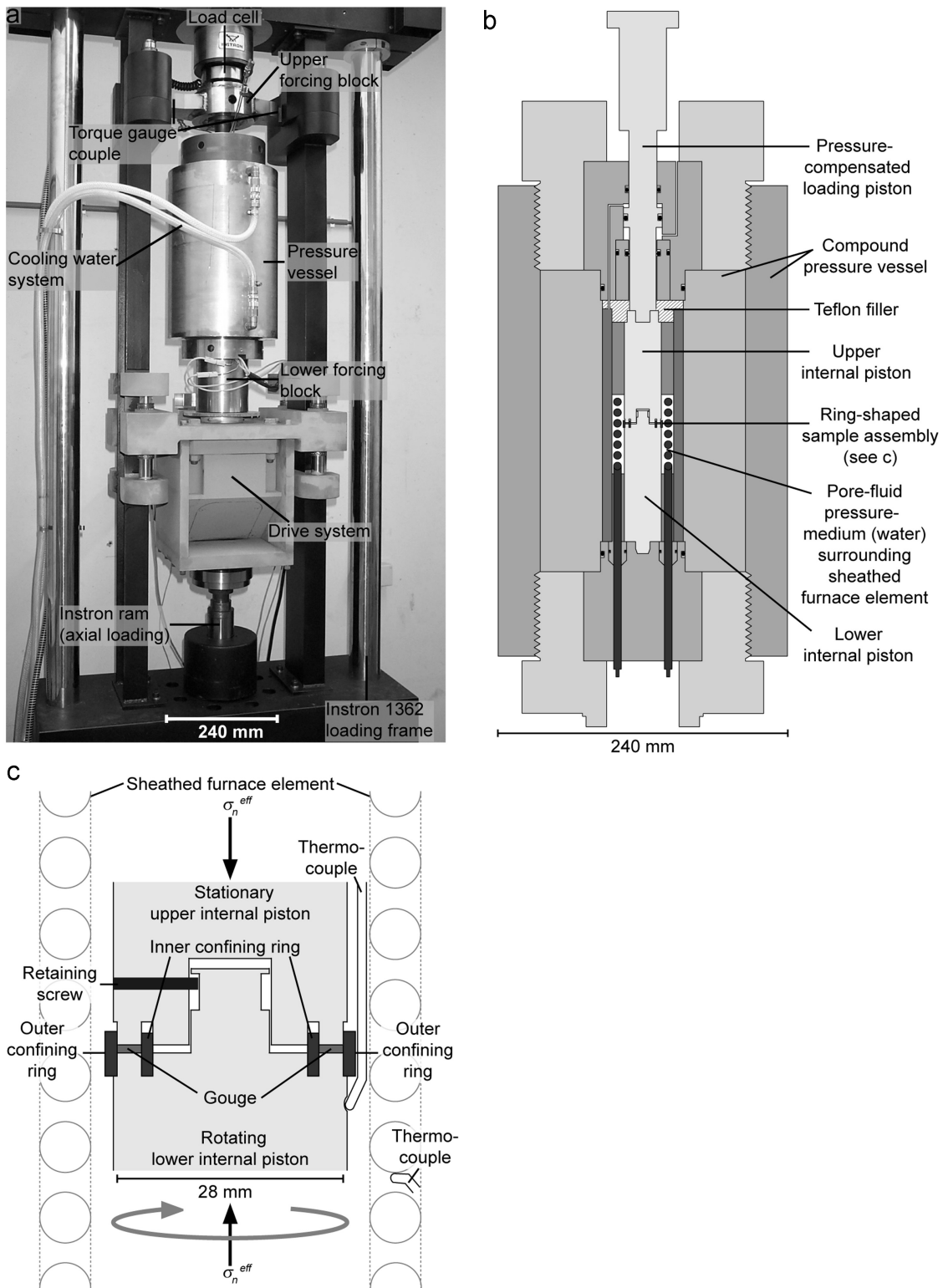


Figure 6: Rotary shear apparatus (Den Hartog et al., 2012)

locked together by a retaining screw, so that it can be connected to the pressure compensated loading piston, and placed inside the pressure vessel where it locks into a key way. The pressure vessel is then closed, using the upper closure nut after which the cooling water is attached. This set up is loaded in the Instron loading frame using a forklift onto a basal support, or lower forcing block. The top of the piston assembly is then located firmly and rigidly into the upper forcing block. When the assembly is positioned, the fluid pressure line, thermocouple connectors and the position transducer (LVDT) are attached.

During the experiments several parameters are measured. Shear displacement is measured using a potentiometer with a digital resolution of $1,66 \cdot 10^{-5}$ mm geared to the lower (rotating) forcing block. Shear stress is measured externally, with a resolution of 0.03 MPa, using the two load cells mounted on the upper forcing block. Normal stress is measured externally using a 100 kN Instron load cell and can be held constant to within ~ 0.08 MPa. Fluid pressure is measured using a pressure transducer with a resolution of 0.005 MPa. The temperatures of the furnace element and the sample are continuously measured to within 1 °C. Displacement and hence compaction/dilatation normal to the simulated fault gouge is measured externally using the LVDT of the Instron loading ram, correcting for the machine stiffness. In this research I only used the small LVDT which has a resolution of $0.13 \cdot 10^{-4}$ mm.

5.2 Microstructural analyses

All thin sections were analysed using a petrographic microscope to inspect the thin sections for localization features, grain size reduction and possible crystallographic preferred orientation (CPO) and if possible look for indications for the operation of pressure solution. All microscopic pictures were taken with crossed polarised light or a gypsum plate which give the most information.

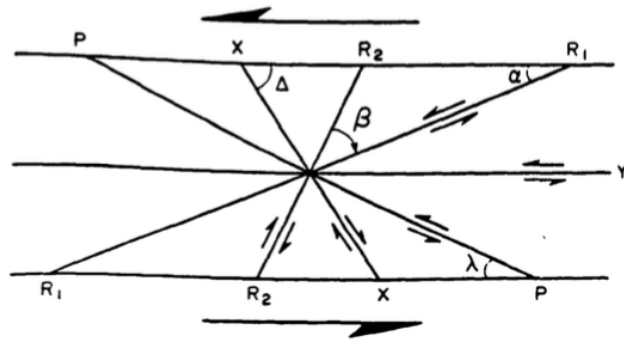


Figure 7: Fracture array and geometrical relationships defined by experiments on simulated fault gouge deformed in triaxial compression (Logan et al., 1992).

The microstructures are compared with the fracture array and geometrical relationships defined by results from experiments on simulated fault gouge deformed in triaxial compression as described by Logan et al., 1992.. The average angles as indicated by figure 7 are 15° for α , 53° for β , 72° for σ , and 16° for λ . In the experiments of Logan et al., 1992, initially shearing is homogeneously distributed across the gouge thickness. Then, shear localizes to riedel shears, both R_1 at about 15° angle to the boundary and R_2 at about 70° angle to the boundary. After this, P fractures might initiate at an about 15° angle to the boundary, but in the opposite direction. Lastly, y shears form, along which most

of the shear takes place. They are parallel and close to the boundary, in the latter case they are called boundary (B) shears.

The stress state within the ring shear is complex, so the microstructures could show slightly conflicting structures and it is not certain if the sense of shear is dextral or sinistral. While the direction of shear within the ring shear is dextral, it depends on the direction from which you look at the sample if it is seen as dextral or sinistral. Looking from the outside in, the structure would

appear dextral, while looking from the inside out, the structure would appear sinistral. This makes defining the fractures in the samples more difficult. However, p shears are rare and hard to see if present, therefore all fractures at an angle of approximately 15° are identified as R₁ fractures, unless mentioned otherwise (Logan et al., 1992).

5.2.1 EDS

Backscattered electron (BSE) images and energy-dispersive x-ray (EDS) maps were acquired on a Zeiss EVO 15 environmental SEM (operated at high vacuum), with double Bruker Xflash 6—30 EDS detector. EDS maps were recorded using Bruker Esprit software and exported as image files.

EDS can be used to produce chemical maps. The signal strength of EDS is determined by three parameters: the accelerating voltage, the probe current and the collection efficiency of the detector. For chemical mapping, which is used in this research, the last two parameters are the important (Allen et al., 2012).

For EDS a coherent focused probe is raster scanned across the thin sections and at each probe position the resultant x-ray emission spectrum is recorded. This spectrum is then used to produce the element maps (d'Alfonso et al., 2010). The phenomenon of x-ray emission is produced by inner-shell excitation with incident electrons. This happens when an inner shell electron transits to a high-energy level and the hole left in the inner-shell is filled by an electron at a high energy level, resulting in emission of a characteristic x-ray with energy between those two energy levels. When the brightness signal corresponding to the characteristic X-ray intensity measured is displayed on the CRT by synchronizing it with the position signal, a two-dimensional X-ray intensity map can be obtained. This observation mode is called the elemental mapping method and is effective for analyzing the distribution of the constituent element in two dimensions (Shindo et al., 2002).

Other images produced were backscattered electron images. These images are produced from electrons from the electron beam that have been elastically scattered. This scattering happens due to the interaction with the atoms in the sample. The heavier the atom, the more backscatter it produces. Therefore, a contrast appears between atoms based on atomic mass.

5.2.2 Microprobe

Compositional analyses of the samples were acquired on a JLEOLJXA-8530F field-emission gun electron microprobe equipped with five tunable wavelength dispersive spectrometers. The operating conditions for the microprobe were 40° takeoff angle, and a beam energy of 20 KeV. The beam current was 10 nA, and the beam diameter was defocused to 1 μm for all spots. The different elements were acquired using different analyzing crystals.

The microprobe does not measure oxygen (O) and hydrogen(H) though oxygen is calculated through cation stoichiometry. After the calculations for oxygen, hydrogen can be determined to obtain a total weight percentage of 100%. The calculations were done by specifying the H:O ratio of the idealized formulae of antigorite and talc.

Serpentine: $Mg_3Si_2O_5(OH)_4$

Talc: $Mg_3Si_4O_{10}(OH)_2$

The idealized H:O ratio are 0.44 and 0.167 for serpentine and talc. If the total weight percentage is approximately 100% with an H:O ratio of 0.44 it means that the mineral at the measured spot is antigorite. The same is true for talc with an H:O ratio of 0.167. For measurements of fine serpentine-

talc intergrowth, H:O was varied between the talc and serpentine endmembers, until total weight percentages between 99.5 and 100.5% were obtained.

5.2.3 FTIR

Infrared (IR) spectroscopy is one of the most common spectroscopic techniques used by organic and inorganic chemists. FTIR is the absorption measurement of different IR frequencies by a sample. The main goal is to determine the chemical functional groups in the sample. Different functional groups absorb characteristic frequencies of IR radiation.

In Fourier transform infra red (FTIR) spectroscopy all frequencies are simultaneously examined. An FTIR exists of a radiation source, an interferometer and a detector. The interferometer produces interference signals, which contain IR spectral information generated after passing through the sample. A mathematical operation known as Fourier transformation converts the interferogram to the final IR spectrum, which is the frequency domain spectrum showing intensity versus frequency. IR spans a section of the electromagnetic spectrum having wave numbers between 13000 to 10 cm^{-1} . At temperatures above zero, all the atoms in molecules are in continuous vibration with respect to each other. When the frequency of a specific vibration is equal to the frequency of the IR radiation detected on the molecule, the molecule absorbs the radiation. Samples for FTIR are prepared by weighing 0,003 gr of finely grained sample and 0,5 gr of potassium bromide powder. Mixing of the sample and potassium bromide is done using an agate mortar and pestle. After mixing, the mixture is pressed into a transparent disk with a mini press using a pressure of 400 bar. Due to moisture absorption during preparation, the IR spectra exhibit bands at 3450 cm^{-1} and 1640 cm^{-1} . To overcome this problem a background measurement is done of only potassium bromide (Hsu et al., 1997).

5.3 Perple_X

Perple_X is a collection of Fortran77 programs for calculating and displaying phase diagrams, phase equilibria, and thermodynamic data (Technology Zurich, n.d.). In this research Perple_X 6.6.9 is used to calculate phase diagrams for antigorite and the transition into its breakdown products. To produce the phase diagrams, I used the composition of antigorite calculated with the microprobe found in table 1 but taking H₂O to be saturated. The initial compositions of the quartz antigorite mixture used for the phase diagrams was calculated with the Rock Maker tool. Rock Maker is a simple software tool that computes bulk rock compositions resulting from mixing or unmixing of rocks or minerals (Büttner, 2012). Because I am interested in the production of talc from a mixture of antigorite with 5 or 10% quartz two phase diagrams were calculated, figures 8 and 9. The phase diagrams were calculated using the hp02ver.dat datafile by Holland et al. and the solution_model for solid solution phases. The diagrams show all products that can be present at the temperature and pressure conditions indicated by the lines.

The two calculated phase diagrams show little difference between them. This would suggest that during all experiments executed with starting materials containing quartz, 5 or 10%, talc would be stable and could be produced from a temperature of approximately 100°C. A second observation is that pressure does not have a significant effect on the production of talc.

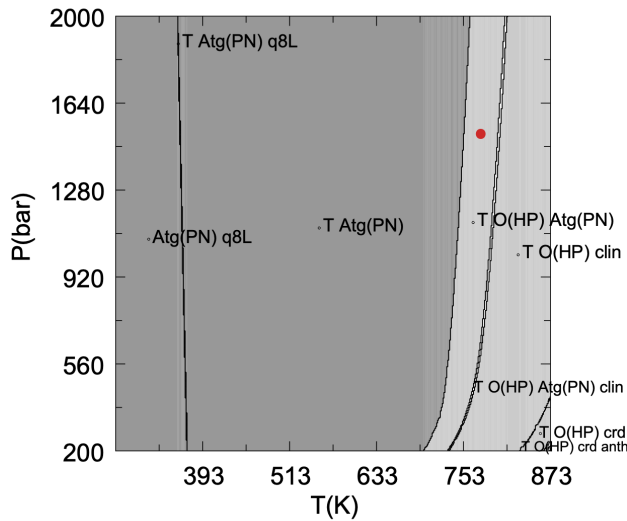


Figure 8: Calculated phase diagram modeled with 5% added quartz.

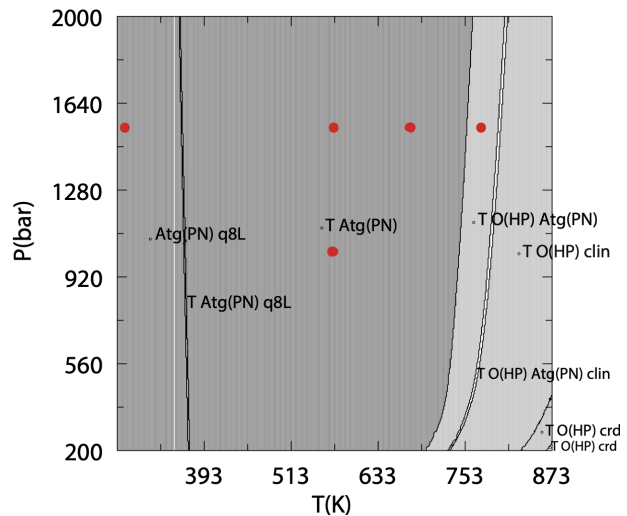


Figure 9: Calculated phase diagram modeled with a quartz percentage of 5%.

Figure 10: Phase diagrams of antigorite into its breakdown products. The red dots are the conditions my experiments were conducted at. q8L is liquid quartz, Atg(PN) is antigorite as written in the solid solution data file, T is talc, O(HP) is olivine as written in the solid solution data file, clin is , crd is cordierite and anth is anthophyllite.

Figure 11 is taken from French et al., 2019. This phase diagram shows the transition of antigorite into its breakdown products taken from Ulmer et al., 1995, produced by using experimental data. Two reactions are added to this diagram. The first reaction, written in purple, is from Wunder et al., 1997 and the second reaction in green is from Irving et al., 1977. When compared to the phase diagrams produced with `perple_x` they do not compare. One reason is because my calculations were performed with a pressure range from 0.02 GPa to 0.2 GPa which is smaller than the 0-3 GPa in figure 11. Looking at the lower part of the diagram the difference is that the temperature at which talc would form is at 500°C while figure 8 and 9 show talc production from 100°C. The forsterite formed in their diagram is due to the starting material containing brucite.

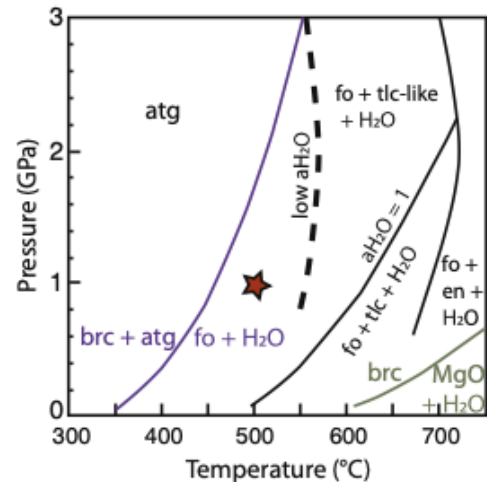


Figure 11: phase diagram for the transition of antigorite to talc (French et al., 2019, Perrillat et al., 2005)

6 Results

Table 2 shows the experiments that were conducted during this research. For all experiments the conditions are listed. For the slow experiments, with velocities of $0.01 \mu\text{m/s}$, also the steady state friction is listed. These values give a quick overview in the difference between the different conditions, especially temperature. The amount of quartz listed in the table and throughout the results are weight percentages.

6.1 Slow experiments

The friction versus displacement plots show how friction evolves during shearing of the samples. Figure 12 shows the friction of all experiments done with a quartz percentage of 10%. These experiments were all conducted at different temperatures, from room temperature up to 500°C . All experiments started at a velocity of $1 \mu\text{m/s}$ for 1 mm after which the velocity was decreased to $0.01 \mu\text{m/s}$ until steady state was reached. All experiments exhibit an initial stage of elastic loading and strain hardening followed by strain weakening. Figure 12 shows very clearly that friction decreases with increasing temperature and that initial strain hardening and peak friction of the experiments is not uniform. The experiments at 20, 300 and 400°C have a peak of strain hardening at 0.52, the experiment at 200°C has a peak at 0.495, and at 500°C the peak is at 0.508. Secondly, when the velocity was stepped down from $1 \mu\text{m/s}$ to $0.01 \mu\text{m/s}$ the experiments at 25 and 200°C have a slight increase in friction before it weakens. At higher temperatures the friction decreases immediately after the velocity was dropped to $0.01 \mu\text{m/s}$. The immediate effect of velocity downstep on the sample gets faster with increasing temperature.

After steady state was reached during the experiments, the velocity was stepped up one time to $0.03 \mu\text{m/s}$ with the exception of the experiment at 20°C (u866), in which the velocity was further stepped up to 0.1, 0.3 and $1.15 \mu\text{m/s}$, and the experiments at 200 and 400°C (u864 and u860), in which the velocity was stepped back down to $0.01 \mu\text{m/s}$ (see table 2). The velocity step from 0.01 to $0.03 \mu\text{m/s}$ caused velocity strengthening in all experiments. When the velocity was stepped back down for the experiments at 200 and 400°C , friction decreased again to the steady state value measured at $0.01 \mu\text{m/s}$ (see table 2). The additional velocity steps for experiment u866 to 0.1 and $0.3 \mu\text{m/s}$ caused a similar velocity strengthening, while the last step up to $1.15 \mu\text{m/s}$ produced velocity weakening. Experiment u888 was only conducted at a velocity of $0.01 \mu\text{m/s}$ but after steady state friction was reached the temperature was dropped from 500 to 20°C . This drop in temperature will be discussed later. The friction at steady state of experiment u888 is 0.238 which is slightly higher than the 0.216 of experiment u865.

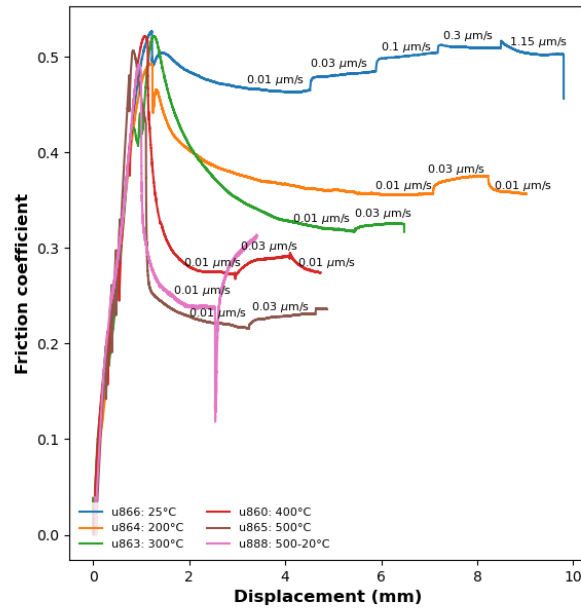


Figure 12: Friction versus displacement. The experiments are conducted with 10% quartz at different temperatures and velocity steps.

Table 2: experiments conducted and their conditions

Experiment	composition (%)	normal stress(MPa)	temperature (°C)	velocity ($\mu\text{m/s}$)	friction at 0.01 ($\mu\text{m/s}$)
u859	90%atg + 10%qtz(outside gouge)	150	400	1 for 1mm - 0.01 - 0.3	0.457
u860	90%atg + 10%qtz	150	400	1 for 1mm - 0.01 - 0.03 - 0.01 for 0,5mm	0.273
u863	90%atg + 10%qtz	150	300	1 for 1mm - 0.01	0.318
u864	90%atg + 10%qtz	150	200	1 for 1mm - 0.01	0.357
u865	90%atg + 10%qtz	150	500	1 for 1mm - 0.01	0.216
u866	90%atg + 10%qtz	150	25	1 for 1mm - 0.01 - 0.03 - 0.1 - 0.3 - 1.15	0.46
u867	pure antigorite	150	300	1 for 1mm - 0.01	0.508
u868	90%atg + 10%qtz	100	300	1 for 1mm - 0.01	0.294
u870	95%atg(25-45 μm) + 5%qtz	150	500-20	1 for 1mm - 0.01 - 0.03 - 0.01 - 0.03 - 1	0.217
u875	pure antigorite	150	25-100-200-300-400-500	1-3-10-30-100 every T	
u877	90%atg + 10%qtz	150	25-100-200-300-400-500	1-3-10-30-100 every T	
u883	95%atg + 5%qtz	150	25-100-200-300-400-500	1-3-10-30-100 every T	
u885	95%atg + 5%qtz	150	500-20	1 for 1mm - 0.01 - 0.03 - 0.01	0.332
u888	90%atg + 10%qtz	150	500-20	1 for 1mm - 0.01	0.238
u894	pure antigorite	150	500	1 for 1 mm - 0.01	0.625 (stick slip)
u899	90%atg(25-45 μm) + 10%qtz	150	500 - 20	1 for 1mm - 0.01	0.216

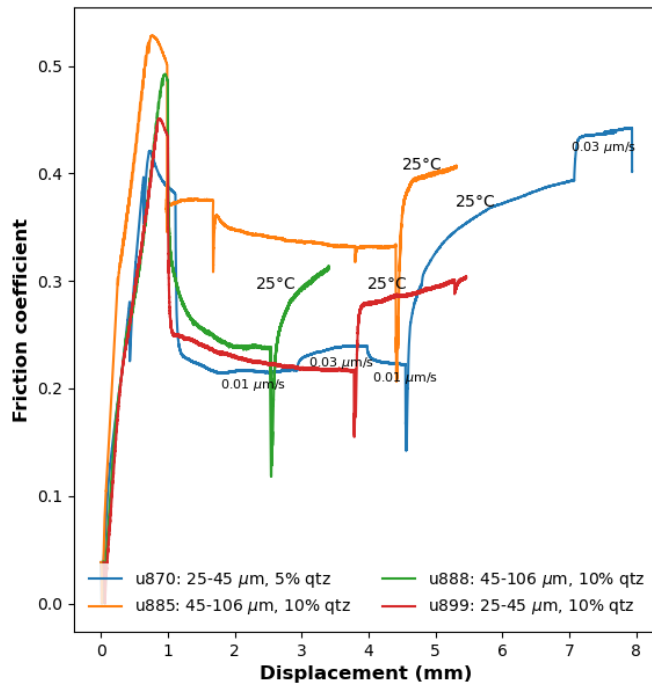


Figure 13: Friction versus displacement for experiments u870, u888 and u899. All at 500°C and 150 MPa but with different grain size or quartz percentages. Experiment u885 has one drop of friction right before steady state friction which is caused by a manual increase of pore fluid pressure.

Another factor that was changed was the grain size. Figure 13 shows friction versus displacement of experiments u870 and u885, u888 and u899. All experiments were conducted at 500°C and 150 MPa with different grain sizes or quartz percentages. u870 and u885 were conducted with a quartz percentage of 5%. The orange line, experiment u885, is conducted with antigorite that had a normal grain size of 45-106 μm while the blue line, experiment u870, is conducted with antigorite that had a grain size of 25-45 μm . There is a significant difference in the friction of the two experiments. The experiment with a smaller grain size has a lower steady state friction than the experiment with a bigger grain size and is of the same level as that in experiment u865 with antigorite with a grain size of 45-106 μm and a quartz percentage of 10%. Experiment u870 also had two velocity steps to 0.03 $\mu\text{m/s}$ and back to 0.01 $\mu\text{m/s}$ which shows that at small grain size it shows velocity strengthening

behaviour and friction decreases again when velocity decreases.

Figure 13 also shows the evolution of friction of experiment u888. Comparing u885, which had a quartz percentage of 5% with u888, which had a quartz percentage of 10% shows that u888 has a lower steady state friction and secondly, that after strain hardening it weakens much faster than experiment u885.

The fourth experiment shown in figure 13 is u899. this experiment was conducted with a grain size of 25-45 μm and a quartz percentage of 10%. Steady state friction at 500°C is 0.216 which, looking at table 2, is equal to the values of experiments u870 and u865. When comparing to u885 with the same grain size but a different percentage of quartz, the steady state friction is lower.

For all experiments in figure 13 the temperature was decreased to room temperature after steady state friction was reached at a velocity of 0.01 $\mu\text{m/s}$. This decrease was executed to see if the low strength of the simulated fault gouges achieved at 500°C would persist at room temperature. For experiments u885 and u888 the friction increases though, it does not go back to the friction that was measured during experiment u866. A second observation is that for experiments u885 and u888 increases of friction are approximately the same, 0.076 for u885 and 0.072 for u888. When looking at experiment u870 the friction also increases when decreasing the temperature, though the friction increase is higher than experiments u885 and u888 with an increase in friction of 0,173 at a

velocity of $0.01 \mu\text{m/s}$. This increase is more than double the increase of the other two experiments. However, The steady state friction at room temperature of both experiments with the smaller grain size are comparable (i.e. u870 and u899). The second observation is the increase in friction when temperature is dropped from 500°C to room temperature. For experiment u899 this difference in friction between 500 and 20°C is $0,084$ while experiment u870 and u888 have a value of $0,173$ and $0,072$. Microstructural analyses on these samples can give a better inside on the difference between the three experiments.

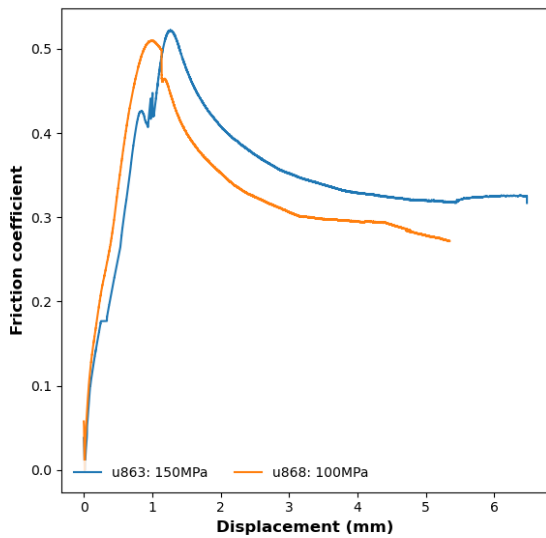


Figure 14: Friction versus displacement of experiments u863 and u868. conducted at 300°C at 150 and 100 MPa.

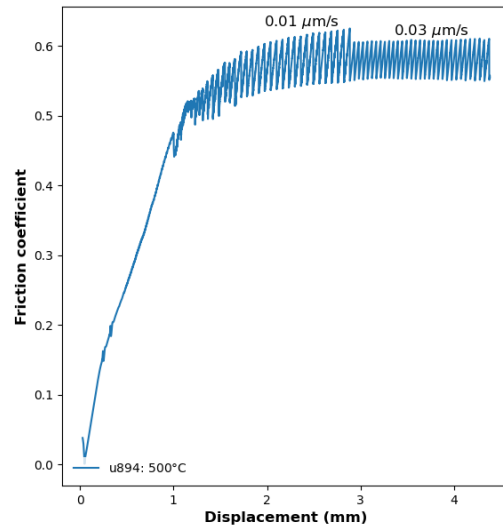
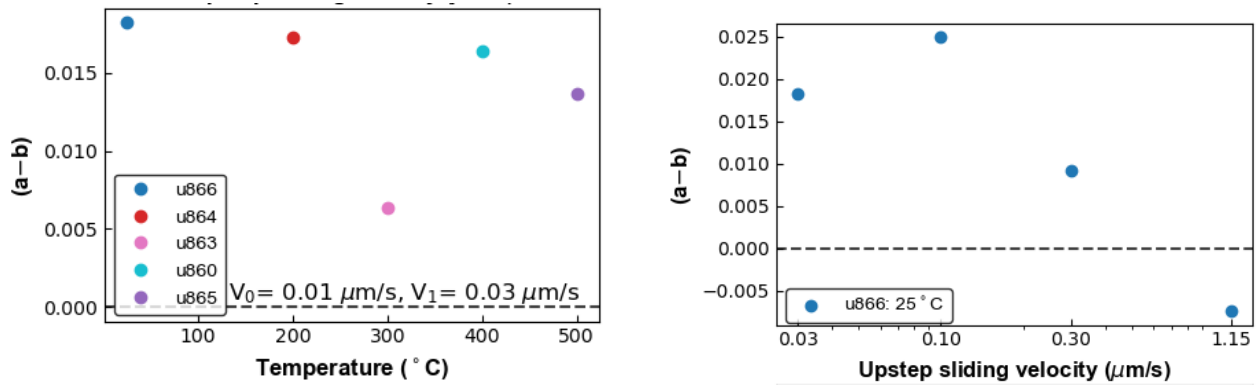


Figure 15: Friction versus displacement for experiment u894, conducted at 500°C with no quartz.

One experiment was conducted with a normal stress of 100 MPa, experiment u868. Figure 14 shows the friction versus displacement graph for this experiment and included is experiment u863 for comparison. both experiments were conducted at 300°C but u863 had a normal stress of 150 MPa. As seen in the graph, friction of experiment u868 is lower than for experiment u863. Secondly, the initial stage of elastic loading and strain hardening ends faster for u868.

The friction development of experiment u894 is shown in figure 15. This experiment was conducted with pure antigorite with a grain size of $45\text{-}106 \mu\text{m/s}$. Friction increased near linearly initially, reached a peak strength and then suddenly drops. This near-linear increase and sudden drop in friction (stick-slip behaviour) repeats with ongoing displacement with increasing friction drops that reach a level of 0.625 . Upon an increase in sliding velocity to $0.03 \mu\text{m/s}$, the friction drops decrease to a value of 0.605 , mainly due to a decrease in the peak friction. This is the only experiment I conducted that showed stick-slip behaviour.

Figure 16a shows the (a-b) values for the experiments from figure 12. It shows that (a-b) slowly decreases with increasing temperature except for experiment u863 at 300°C , which has a significant lower value than the other experiments. Figure 16b shows the (a-b) values for experiment u866 conducted at room temperature. Only the highest V1 of $1.15 \mu\text{m/s}$ has a negative value and could induce stick slip behaviour.



(a) (a-b) versus temperature for experiments conducted with 10% quartz at different temperatures.

(b) (a-b) versus velocity for experiment u866.

Figure 16: (a-b) values for experiments with $V_1=0.03 \mu\text{m/s}$ and experiment u866.

The (a-b) value for u894, which is not plotted in the figures, is -0.0109 and is a negative value. This is the only negative value for the slow experiments.

6.2 Fast experiments

Three experiments were conducted at faster velocities to give an insight in the velocity dependence of (a-b). These experiments started at room temperature and continued with temperature steps of 100, 200, 300, 400 and 500°C. At each temperature step five velocity steps were set: 1, 3, 10, 30 and 100 $\mu\text{m/s}$. At room temperature velocity started at 1 $\mu\text{m/s}$ for 5mm. The experiments then continued with the next velocity steps, shearing the sample with a total displacement of 14 mm at room temperature. The next temperature steps made a total displacement of 10.5 mm where the displacement was 1.5 mm for velocity steps 1,3 and 10 $\mu\text{m/s}$ and 3 mm for 30 and 100 $\mu\text{m/s}$.

Figure 17 shows the friction versus displacement plots for all three experiments. U875, containing no quartz, shows a velocity weakening at room temperature and is the only experiment that shows an increase in friction with increasing temperature throughout the experiment. Experiment u877, containing 10% quartz, also shows

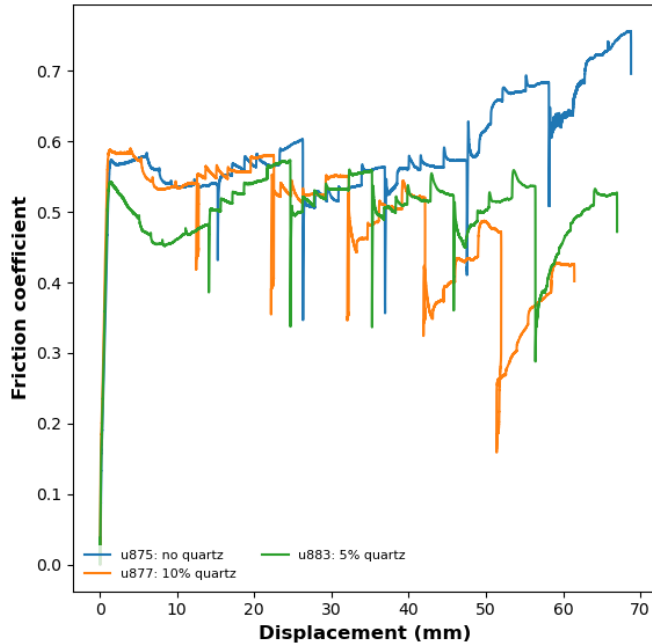


Figure 17: Displacement versus friction of experiments u75, u877 and u883.

Experiment u877, containing 10% quartz, also shows

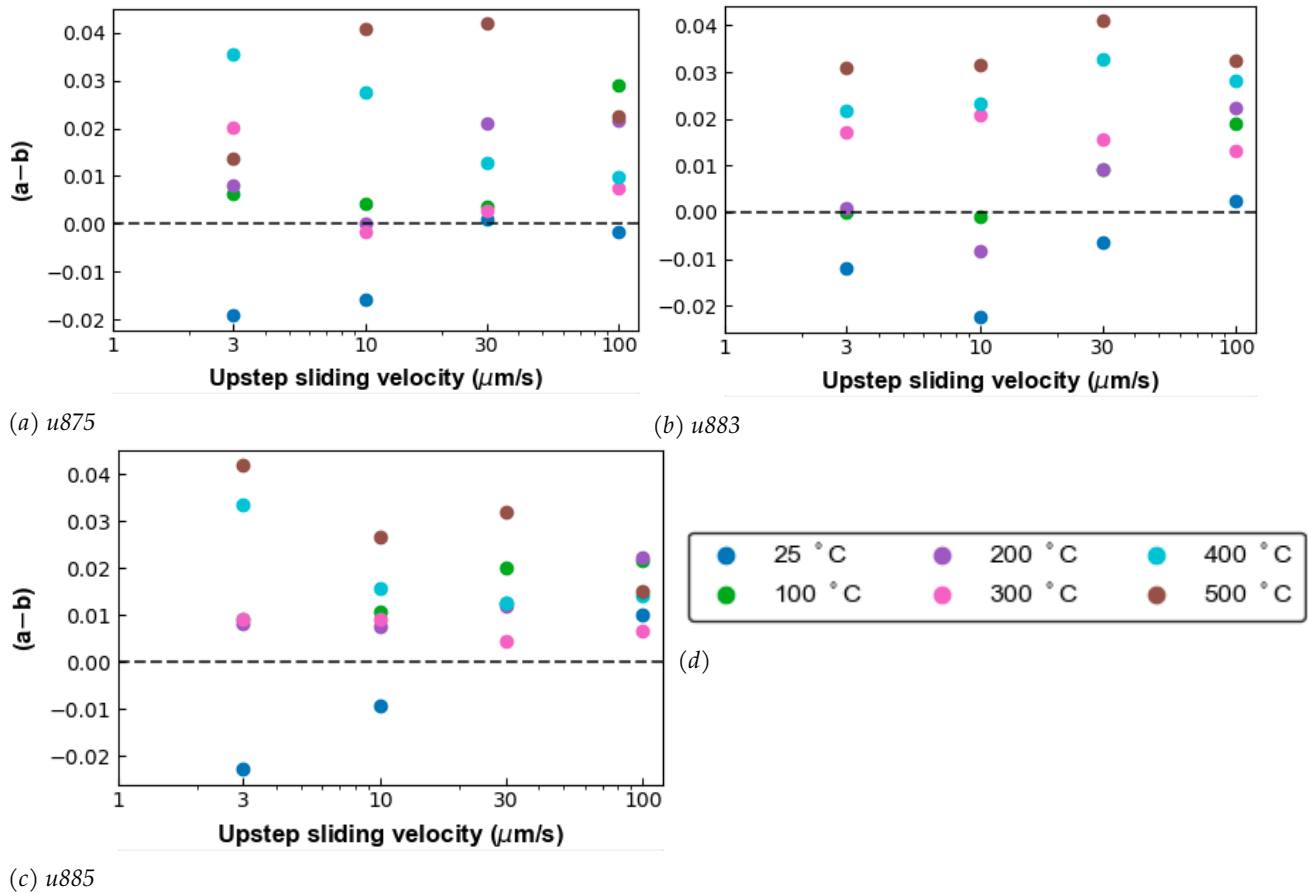


Figure 18: (a-b) versus velocity for experiments a) u875 of pure antigorite, b) u877 containing 10% quartz, The values at an upstep velocity of 30 $\mu\text{m/s}$ for temperatures of 100 and 200°C are the same, and c) u883 containing 5% quartz.

velocity weakening at room temperatures. Though, from a temperature of 100°C it is velocity strengthening and has a decreasing friction with increasing temperature. U883, containing 5% quartz, shows almost the same friction evolution as experiment u875 with velocity weakening at room temperature, but the decrease in friction with increasing temperature start at 200°C. Another observation is that the difference in friction between the temperature steps is much bigger during experiment u877 than experiment u883. Though, the difference in friction is bigger for the temperature steps the difference in friction between the velocity steps stay approximately the same.

Figure 18 shows plots where (a-b) is plotted against velocity. The first observation is that (a-b) increases with increasing temperature, with a few exceptions. The second observation is that most (a-b) values at room temperature are negative and therefore could initiate stick slip behaviour. Though, this did not happen, looking at figure 17. Furthermore, (a-b) changes with velocity. At low temperatures (a-b) gets higher at increasing velocities and at the high temperatures (a-b) decreases with increasing velocity.

figure 19 shows the same (a-b) values but plotted against temperature. These plots show that at 300°C and a V1 of 100 $\mu\text{m/s}$ the (a-b) drops and then increases again with increasing temperature. While for the lowest V1, (a-b) increases with temperature without any sudden drops. For V1=10

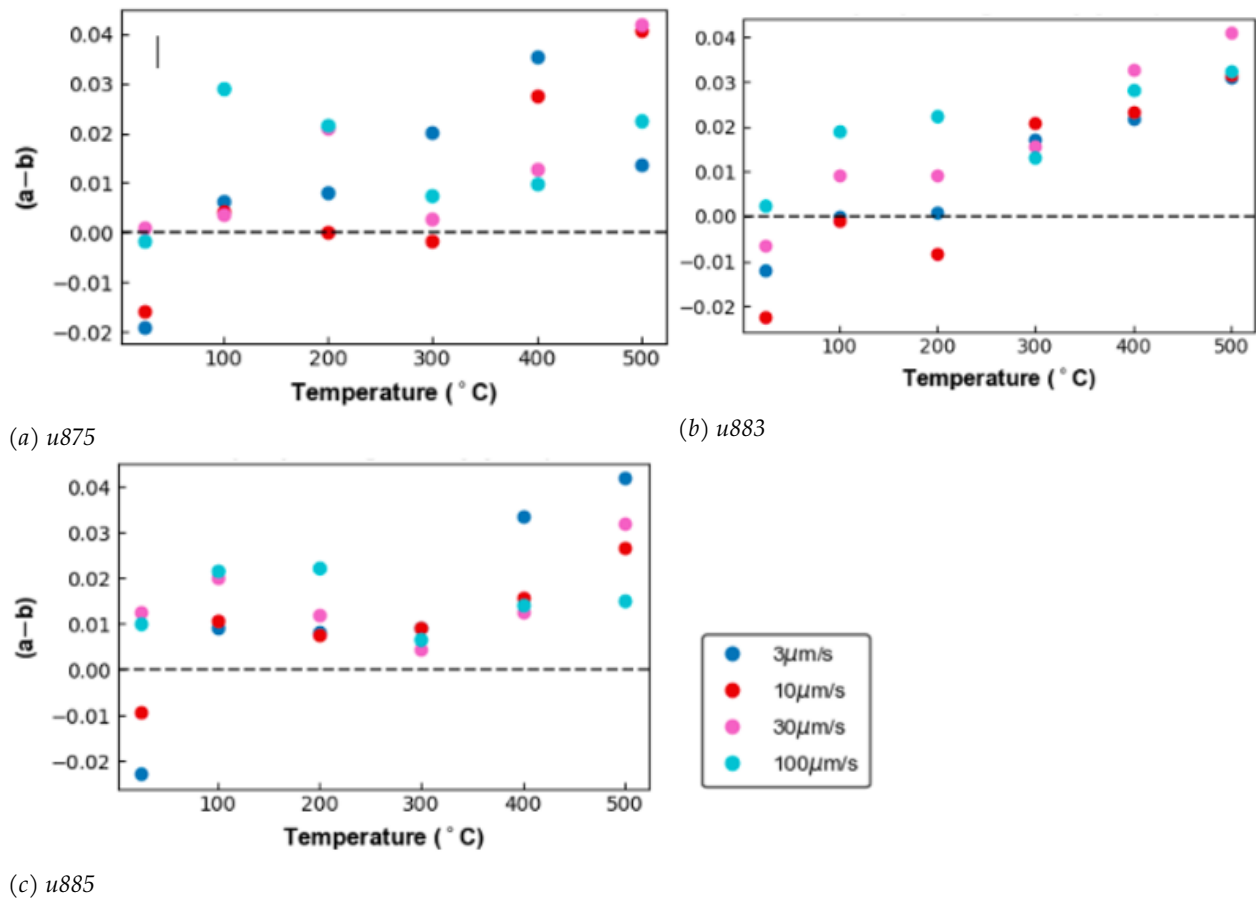


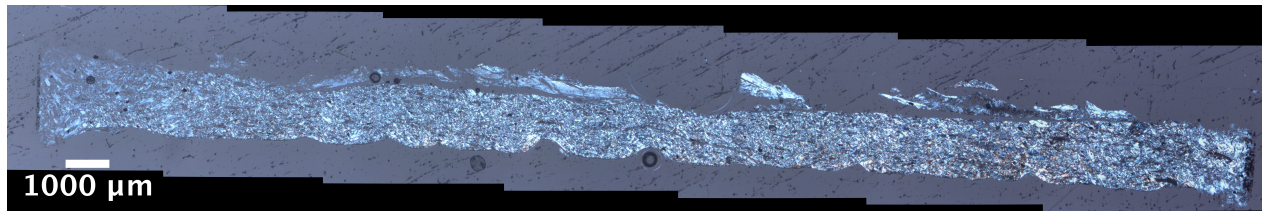
Figure 19: (a-b) versus temperature for experiments a) u875 of pure antigorite, b) u877 containing 10% quartz, and c) u883 containing 5% quartz..

and 30 $\mu\text{m/s}$ the values also drop but this drop is or at 200°C or at 300°C. For experiment u877 the drop for both $V1=10$ and 30 $\mu\text{m/s}$ is at 200°C. Another observation that confirms the trend in figure 18 is that the velocity dependence of (a-b) changes as the temperature increases. At temperatures of 25, 100 and 200°C the highest (a-b) value is, with a few exceptions, at the highest velocity. After the drop in (a-b) discussed, the (a-b) value of 100 $\mu\text{m/s}$ gets lower at increasing temperature relative to the other velocities. However, in general there is an increase in (a-b) with increasing temperature.

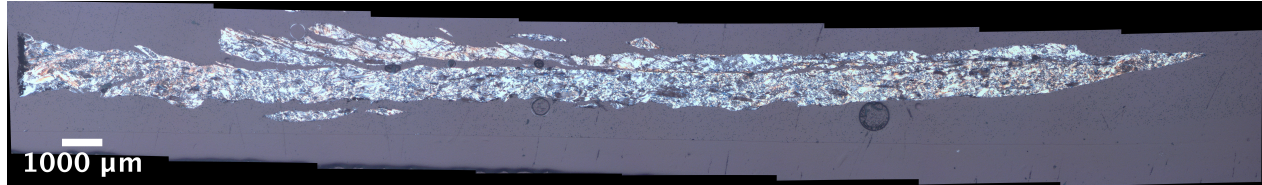
6.3 Microstructures

The following figures show mosaics of light microscopy pictures of several samples containing different percentages of quartz or with antigorite of different grain sizes. Due to the small grain size of quartz of mostly 5 μm it is hard to distinguish in the thin sections. The principle slip zone of the experiments is always the top part of the pictures which is defined by the jagged pattern from the teeth of the piston on the bottom of the spectator region.

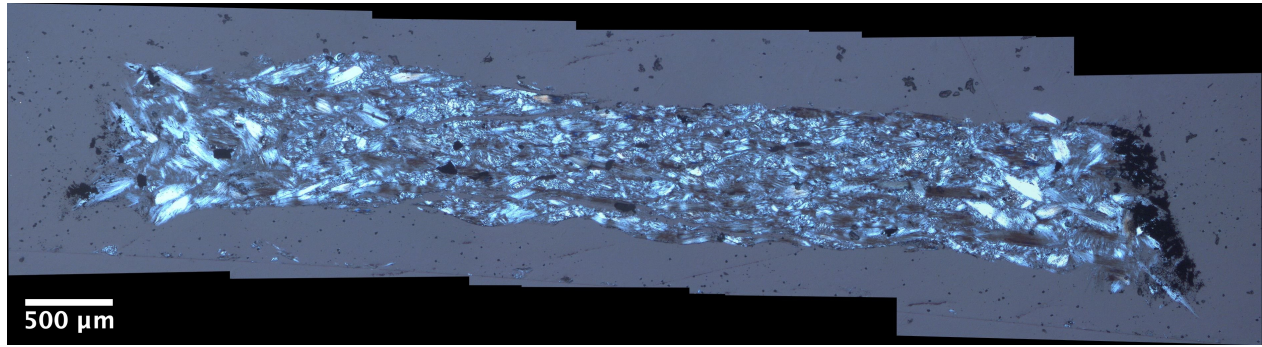
Figure 20 shows cross sections, under crossed polarized light(xpl), of three experiments conducted at 500°C during this research. A) is from experiment u870 which was conducted with a



(a)



(b)



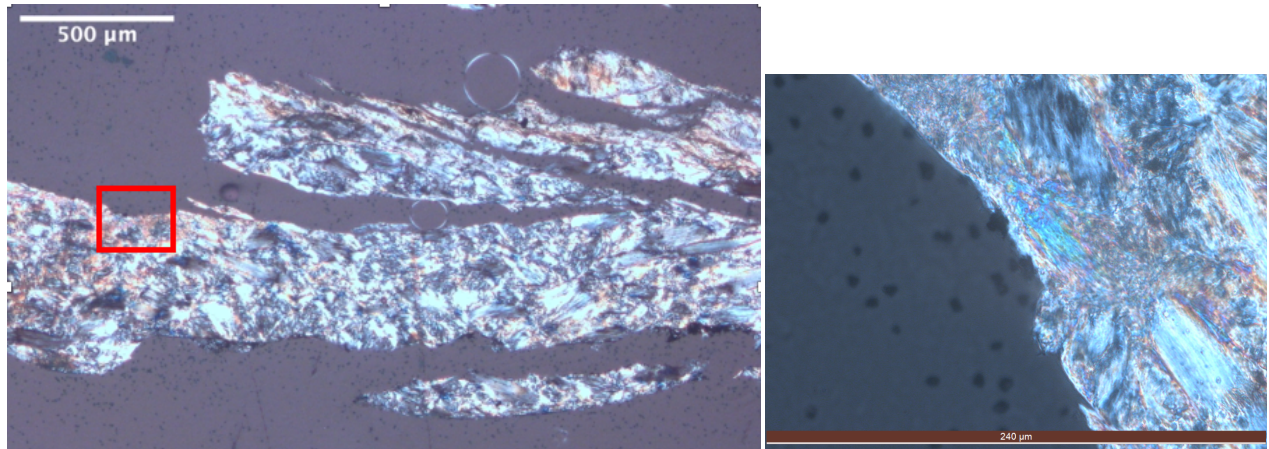
(c)

Figure 20: cross sections under crossed polarized light of experiments a) u870 with the small grain size and 5% quartz, b) u885 with the normal grain size and 5% quartz and c) u894 containing pure antigorite with normal grain size.

grain size of 25-45 μm and a quartz percentage of 5%. A difference is seen between the principle slip zone on top and the spectator region. The grain size of the material in the principle slip zone seems to be even smaller as the rest of the sample and the principle slip zone is also separated from the gouge by a horizontal fracture. R_1 shears within the microscopy picture indicate a dextral sense of shear. B) shows a cross section from experiment u885 conducted with a grain size of 45-106 μm and a quartz percentage of 5%. This one also shows a difference in grain size between the principle slip zone on top and the spectator area of the sample and it seems to have undergone more grain size reduction. Just like the previous cross section the principle slip zone is separated from the rest of the sample by an horizontal over the a great length of the sample. There also seem to be R_1 shears within the principle slip zone that indicate a dextral sense of shear. C) shows a cross section from experiment u894 which was conducted using pure antigorite with a grain size of 45-106 μm and does not shows a principle slip zone like the other experiments and from the cross section it is difficult to specify sense of shear. Experiments u885 and u894 both started from antigorite with a grain size of 45-106 μm . However, after the experiment u885 contains a greater amount of reduced grains as experiment u894, while stick-slip behaviour is normally associated with localized deformation along a boundary shear (the boundary shear might not be recovered from the sample).

Figure 21 shows two microscope pictures under crossed polarized light. On the left side in a)

the grain size is smaller on the left side of the picture and at the top of the principle slip zone than across the rest of the sample. B) is zoomed in on the area marked in figure 21a. The grain size is small and in the middle there is a grain with a high birefringence which can not be antigorite. Antigorite has a first order birefringence and would stay black/grey or brown with sometimes a slight blue glow under xpl, depending on the orientation. Quartz also has a low birefringence and does not show these bright colours in xpl. U885 is the only sample in which a grain with high birefringence is found.



(a) experiment u885 5x magnified, xpl.

(b) experiment u885 40x magnified, xpl.

Figure 21: experiment u885 with different magnifications. B) is the marked area from a.

Figure 22 shows a small section of experiment u894. The thin section shows that at the top of the sample the grain size is further reduced than at the bottom. But the grains are not as reduced as the experiment where quartz is added.

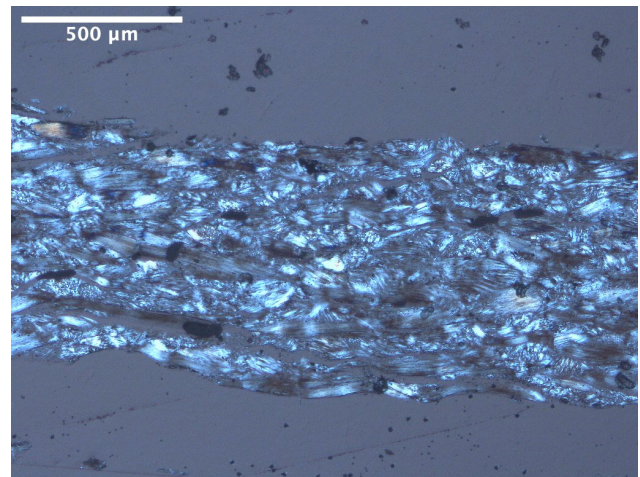


Figure 22: experiment u894 5x magnified, xpl.

Both pictures 23a and 23b show the cross sections for experiment u870 and u885 also seen in figure 20a and 20b but this time with the gypsum plate inserted. These two pictures were chosen because u870 gives a good representation of what is found in almost all thin sections and u885 is shown as an exception. Using the gypsum plate a uniform extinction colour can be distinguished which might indicate a crystallographic orientation (CPO) for experiment u870. Experiment u885 shows a less prominent CPO. Looking at the principle slip zones in these pictures it shows that there is a difference between the principal slip zone and the spectator area which can be due to a difference in CPO but also a difference in grain size. This figure is consistent with all experiments that were examined with a gypsum plate.

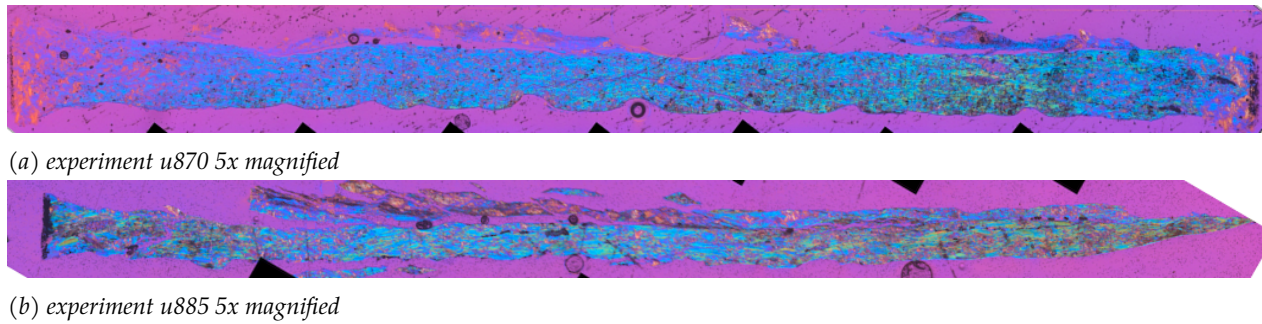


Figure 23: cross sections of experiments a) u870 and b) u885 with the gypsum plate inserted

6.4 Microprobe results

The microprobe was used to analyze the microstructures from experiments u865 and u866. Both samples were conducted under the same conditions aside from the temperature. U865 was conducted at 500°C and u866 at room temperature. 36 spots were analysed on different parts of the sample. Examples of the locations of spot analysis and the corresponding measurements are shown in Figure 26 and Table 3, respectively. Back scattered electron images show that at 500°C, the grains are reduced in size in comparison to grains that were sheared at room temperature, see figure 24 and 25. Fractures in u866 are oriented at an angle of approximately 15° and are probably r_1 shears. Further, the back scattered electron image of u865 shows a difference in grey tones around the edges of antigorite grain fragments and quartz grains (figure 26). The antigorite grains in u866 do not show this and are approximately uniformly grey. Further, looking into the results showed that there is a difference in the O:H ratio (figure 3).



Figure 24: BSE image of u865 with the principle slip zone to the right.

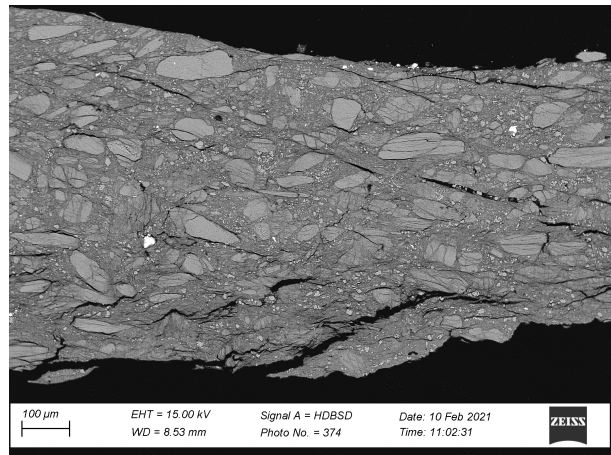


Figure 25: BSE image of experiment u866.

Throughout the measurements oxygen(O) and hydrogen(H) are not measured. The values for O and H are calculated afterwards through stoichiometry as described in section 5.2.2. These calculations give an H:O ratio that is used to test whether antigorite and/or talc is found. Looking at the endmember of antigorite, $Mg_3Si_2O_5(OH)_4$, it contains 9 O atoms and 4 H atoms this means that the

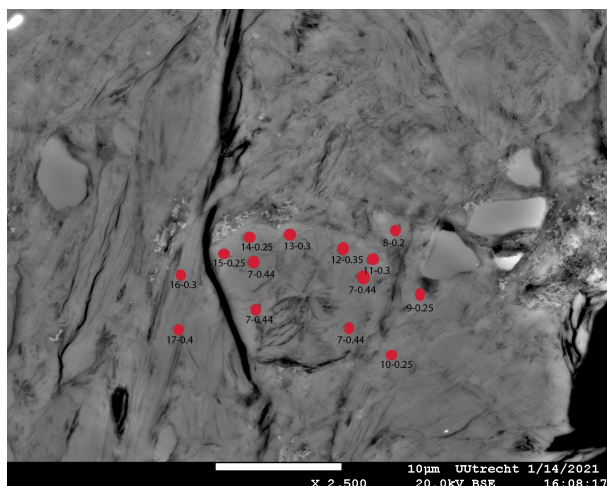


Figure 26: The positions of measurements of sample u865. The text beneath the red dots is the number of the measurement and the H:O ratio of that point.

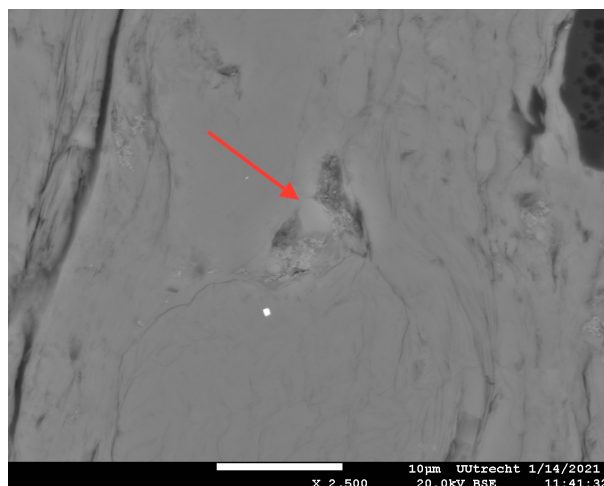


Figure 27: Back scattered electron image of sample u865. Quartz in this grain is surrounded by a "fluffy" layer of presumably talc. The red arrow indicates the quartz grain.

H:O ratio is 0.44. This ratio plus a total of all atoms was 100% means antigorite is found. For sample u866 all grains had a total of approximately 100% with an H:O ratio of 0.44 and thus all antigorite grains. When looking at figure 26 and table 3, the measurements done in the middle of the grain also had a H:O ratio of 0,44, indicative for antigorite. Though, at the grain boundaries, the lighter shades of grey, showed a lower H:O ratio decreasing inwards to the grain. This decrease in H:O ratio means that antigorite is reacting. When looking at the composition of talc, $Mg_3Si_4O_{10}(OH)_2$, the H:O ratio should be 0,167.

Table 3 shows a small overview of the weight percentages that were measured during the microprobe analyses. The elements in the table are the ones that show a reaction took place from antigorite to talc. The H:O ratios of 0.44 show an Si weight percentage of 20,5% to 21,4% while the spots with a lower calculated H:O ratio have a higher weight percentage of Si from 22 to 25,5%. At the same time, the weight percentage of Mg decreases when the H:O ratio decreases, unless the wt% of aluminium is high. For aluminium the weight percentage also decreases when the H:O ratio decreases.

H:O ratio	Si wt%	Mg wt%	Al wt%
0.44	21,23	21,71	0,77
0.44	20,47	22,04	0,80
0.44	21,05	22,02	0,83
0.35	22,09	22,70	0,75
0.3	24,08	20,67	0,55
0.3	22,67	22,76	0,73
0.25	23,14	22,78	0,80
0.25	25,31	19,90	0,65
0.2	25,37	20,91	0,60

Table 3: Weight percentages of the elements: Si, Mg and Al measured at several spots on the sample with various O:H ratios.

6.5 EDS results

In the following, I show images and elemental maps of the microstructures of four samples, namely u865, u870, u885 and u899. All images are an aggregation of multiple measurements which is why there can be a small difference in color within the figures. For all samples a BSE mosaic and element maps covering the width of the gouge layers were produced of which the most important ones are presented here, silica, magnesium or a combination of those two. The figures all show a principle slip zone on top on top of the spectator area.

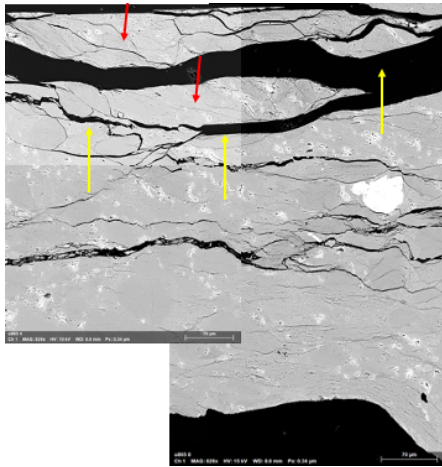


Figure 28: Mosaic of BSE images of sample u865, containing normal grain size antigorite, 10 wt% quartz and deformed at 500°C. The red arrows indicate R_1 shears and the yellow arrows indicate the beginning of the principle slip zone.

Figure 28 shows a mosaic of BSE images of an area in sample u865, conducted with normal grain size and 10% quartz. Figure 28 shows the BSE image. Fractures in the sample are two γ shears in the middle of the sample and at the top separating the principle slip zone from the rest of the sample. Other fractures are R_1 shears mainly within the principle slip zone. Those R_1 shears show that sense of shear in the microstructures is dextral. The second observation is the position of the quartz, which is very light in color and is oriented in an angle of approximately 35° along the shear direction. Figure 29b supports this statement because the bright red spots are quartz and are distributed the same as the bright spots on the BSE image. Individual grains are difficult to distinguish in the BSE mosaic but they can be easily recognized in the Si map and to some extent in the Mg map, see figure 29. Grains in the Si map are characterized by a lower Si percentage than the surrounding area. In the Mg map grains are distinguished by a higher Mg content in the grains than the surrounding area. For all element maps the top, which is the principle slip zone of the sample, has a more homogeneous distribution of the elements and the outlines of grains can't really be identified.

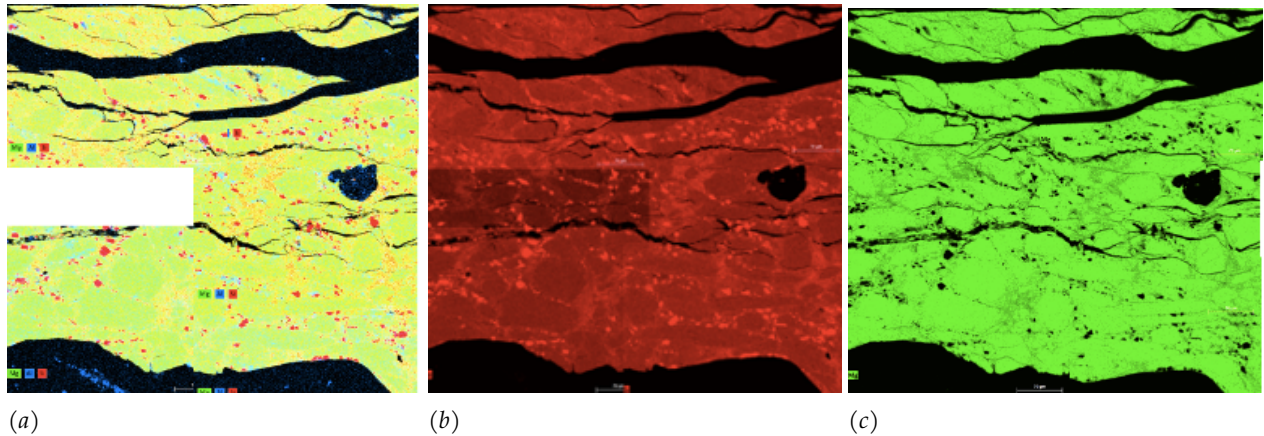


Figure 29: Mosaics of element maps for experiment u865 where a) shows an overlay of the elements Si (red), Mg (green) and Al (blue). B) shows the distribution of silicon throughout the mapped area. C) shows the magnesium distribution throughout the mapped area.

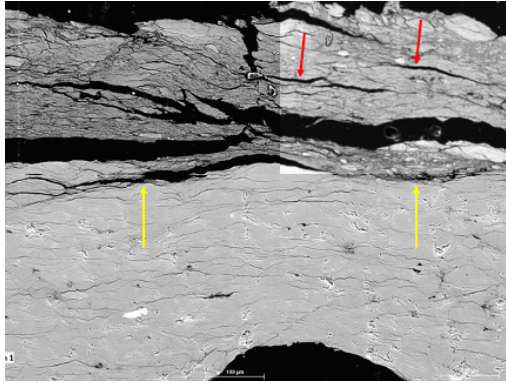


Figure 30: Mosaic of BSE image of sample u870, containing 25-45 μm antigorite, 5% quartz and deformed at 500°C. The red arrows indicate R_1 shears and the yellow arrows indicate the beginning of the principle slip zone.

Figure 30 shows a mosaic of BSE images of an area in sample u870, 25-45 μm antigorite and 5% quartz. This area is used for element maps shown in figure 31. The BSE image shows that fractures in the sample are mostly present within the principle slip zone and are mostly R_1 shears. The sense of shear in these mosaics of BSE and element maps is dextral. The element maps of u870 have one thing in common which is that in the principle slip zone the brightness of the maps is less which is due to all the fractures between the grains. Because of the small grain size used during this experiment and the limited resolution of the acquired maps there are no grains distinguishable. Looking at figure 31a the color is not homogeneous across the sample which means there is a variability in Si:Mg ratio throughout the mapped area.

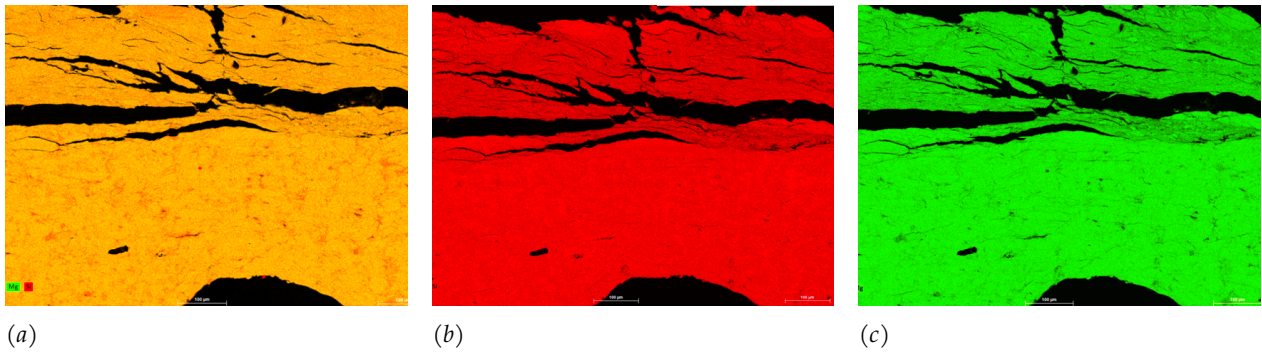


Figure 31: Mosaics of element maps of sample u870, where a) is an overlay of Mg(green) and Si(red), b) is for silicon and c) is for Magnesium.

Figure 32 shows a BSE mosaic of BSE images of an area in sample u885, normal grain size antigorite plus 5wt% quartz. For this experiment two different spots were chosen instead of one area. The chosen spots are indicated by the red squares. These areas were chosen on the basis of findings with the microscope, see figure 21b, the differences of the spot in grain size reduction and fracture distribution within the two different zones. The BSE images show that within the principle slip zone fractures are more prominently present than in the spectator area. Fractures within the principle slip zone suggest a dextral sense of shear in the microstructures. Another observation is that the grains within the principle slip zone are not distinguishable, as seen in figures 33 d-f, whereas the spectator area, figures 33a-c, seems to have a few grains at the top and going downwards the area gets a more homogeneous distribution. Images b) and c) show the same effect as figure 29 where between the few grains the silica content is higher whereas the magnesium content is lower as within the grains. Though this is largely at the top of the sample. Coming back to the microscopy picture in figure 21 the high birefringence is caused by a mineral with a high silicon content and low magnesium content.

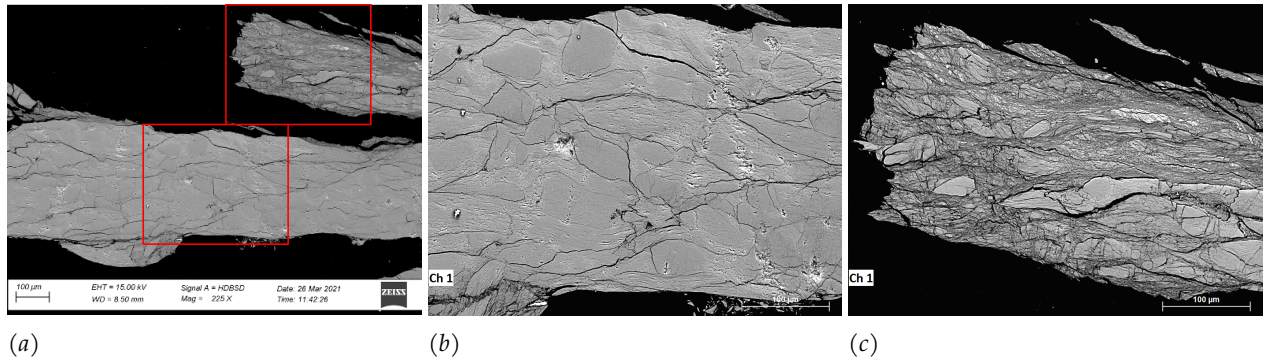


Figure 32: BSE Mosaics of sample u885, conducted with normal size antigorite, 5% quartz and deformed at 500°C. a) is an overview with the red squares being the areas of images b) the left lower square or spectator area and c) the right upper square which is the principle slip zone.

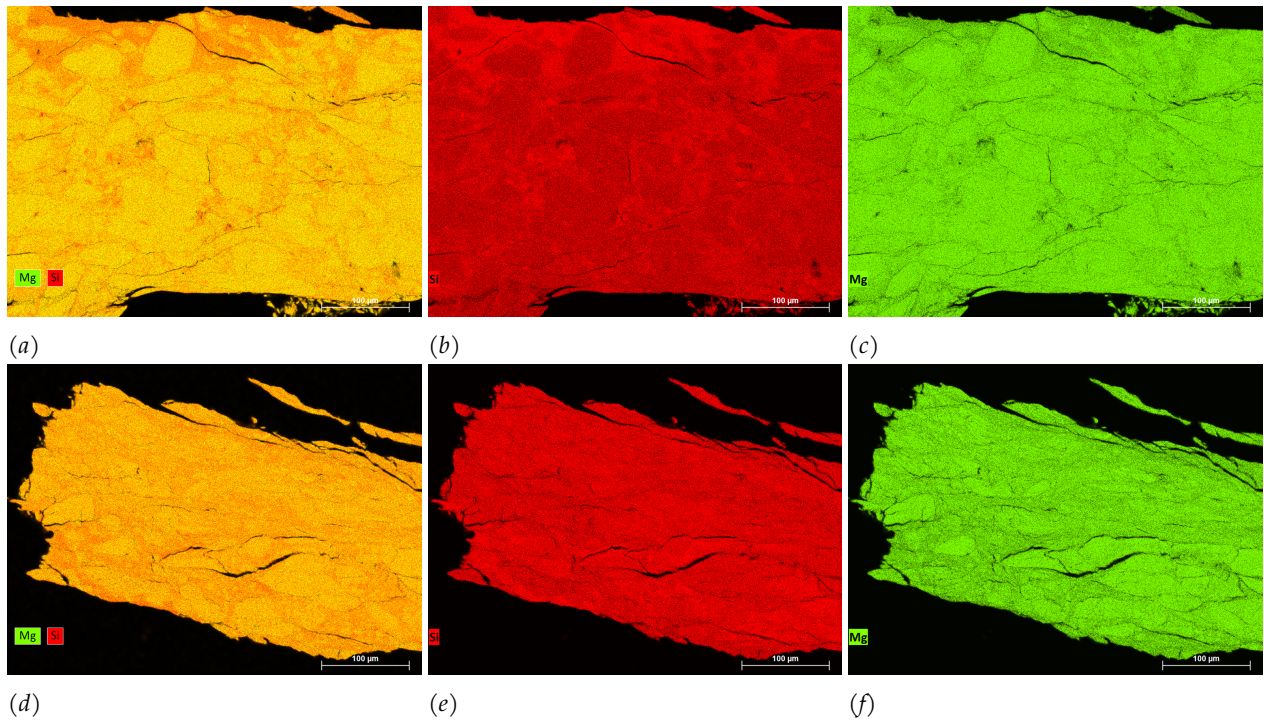


Figure 33: Mosaic of element maps from the mosaic of BSE images from figure 32b and 32c a,b and c are from figure 32b and d,e and f are from figure 32c. a) and d) are overlay maps for Mg(green) and Si(red), b) and e) are Silicon maps and c) and f) are magnesium maps.

Figure 34 shows the mosaic of BSE images of an area in sample u894, normal grain size antigorite and no quartz, and is the area used for the element maps in figure 35. Fractures within the sample are mostly along the distinguishable grains, though there are also R_1 fractures which extent along several grains. These fractures indicate that sense of shear within this microstructure is sinistral. Looking at the BSE image and the Si and Mg maps, grains are distinguishable with in between a lot of grain size reduction. Secondly, looking at the combination map of Si and Mg the color distribution is homogeneous which means there is no variability in the Si:Mg ratio across the sample.

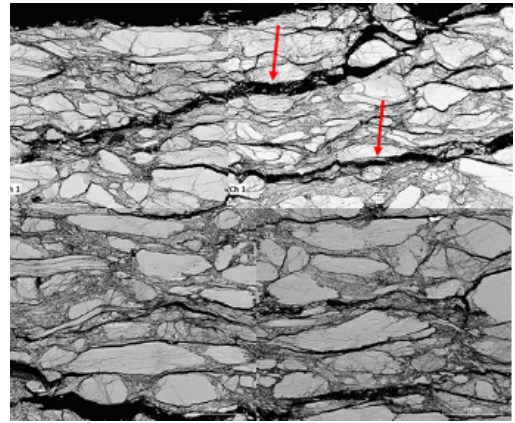


Figure 34: Mosaic of BSE image of sample u870, containing normal size antigorite, no quartz and deformed at 500°C. The red arrows indicate the R_1 shears.

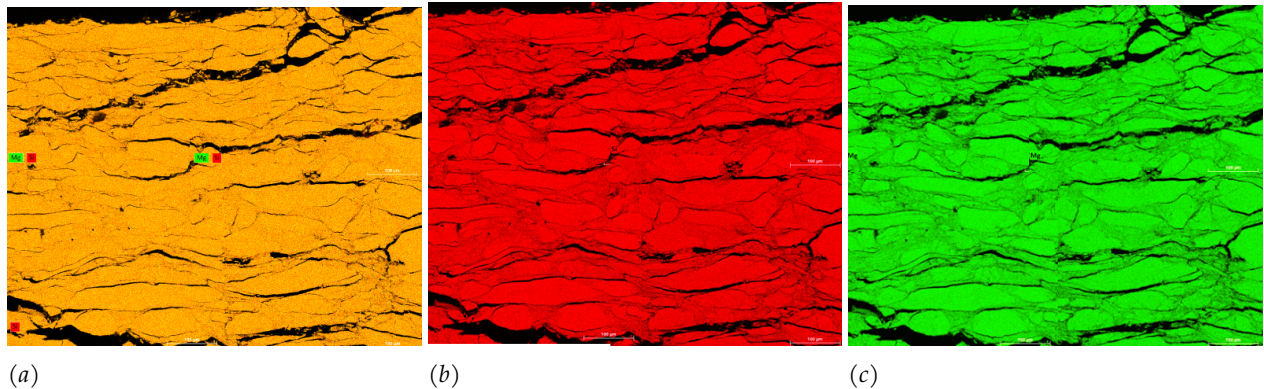


Figure 35: Mosaic of element maps of sample u894, normal grain size and no quartz, where a) is an overlay of elements Mg(green) and Si(red) b) is Si and c) of Mg.

6.6 FTIR results

The results of The FTIR analyses are presented in the graphs below. Figure 36 shows the graph of the two different starting materials with 5% and 10% quartz. For both starting materials, two analyses were done to verify if the quartz and antigorite were properly mixed so every sample did have a quartz percentage of approximate 5 or 10%. As seen in the graph the intensities of the peaks for the different start materials are not proportionate to the relative proportions of quartz and antigorite. However, the intensities of the 10% quartz at reciprocal wavelength 1100 cm^{-1} are higher than the intensity of the peaks for 5%, while the peaks for antigorite at a reciprocal wavelength of 1000 cm^{-1} show a lower intensity than the start material containing 5% quartz. The difference in intensity of the peaks can be due to different amounts of material in the starting material.

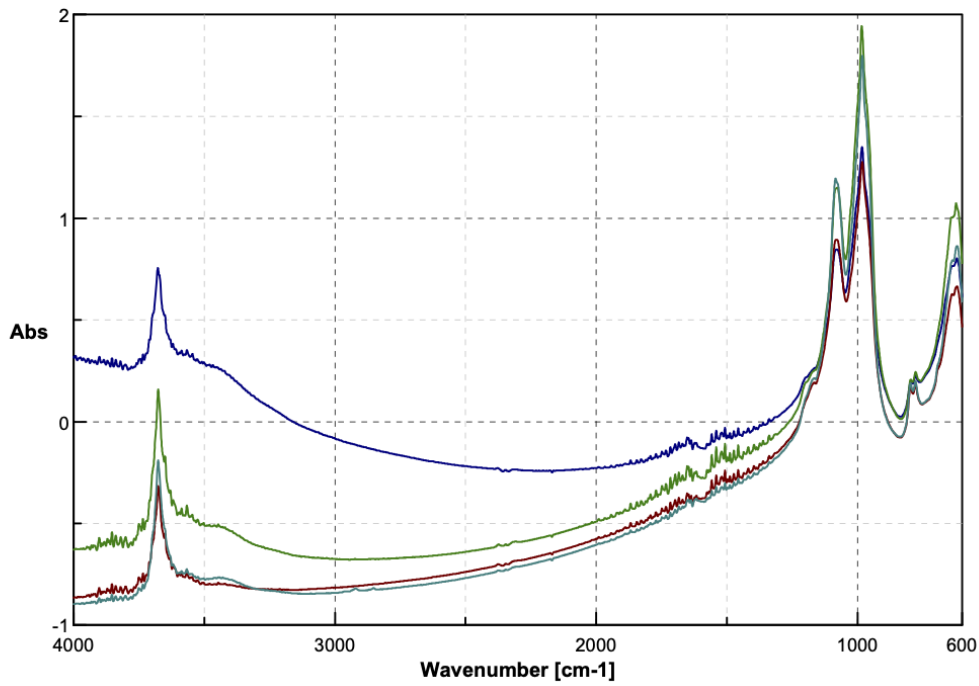


Figure 36: FTIR measurements of the start material with 10% quartz (green and dark blue lines) and 5% quartz (light blue and red lines).

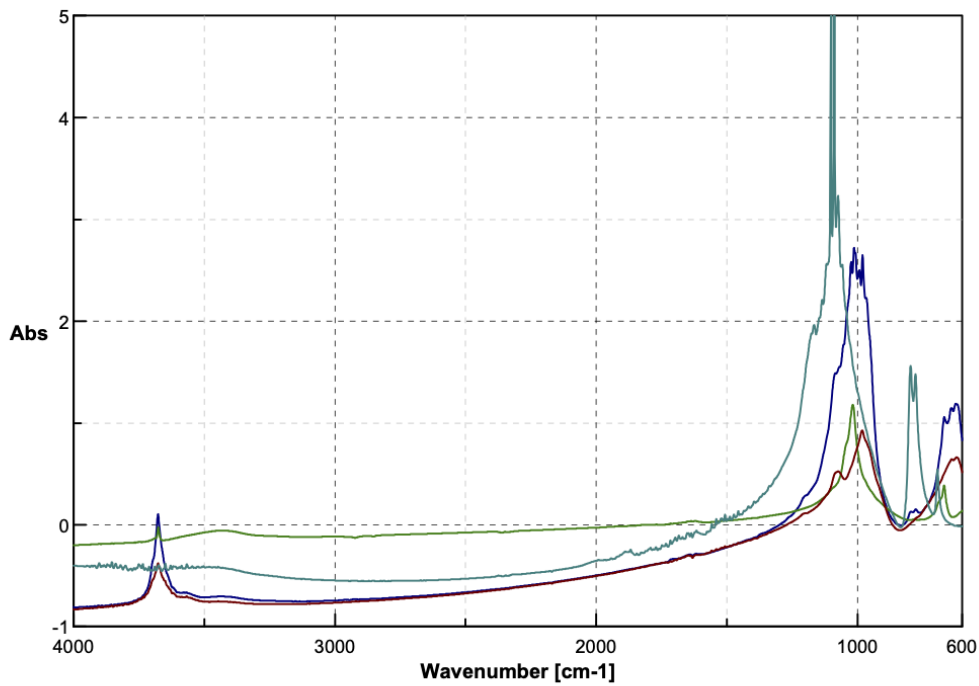


Figure 37: FTIR measurements of sample u865 (blue line), quartz (light blue line), talc (green line) and antigorite (red line).

Figure 37 shows the analyses of experiment u865 together with the analyses for antigorite, quartz and talc. Which shows that sample u865 has peaks at 3700 cm^{-1} , 1000 cm^{-1} and 650 cm^{-1} which correspond to antigorite. There are also peaks at 1050 cm^{-1} and 700 cm^{-1} for talc and low intensity peaks for quartz at 1100 cm^{-1} and 750 cm^{-1} . This graph confirms that talc is formed during the experiment at 500°C .

The following two figures of FTIR measurements show the spectra of samples u865, u870, u885 and u894. All these experiments were conducted at 500°C , a normal stress of 150 MPa and a velocity of $0,01\ \mu\text{m/s}$.

Figure 38 shows samples u865, u885 and u894. The starting material of these experiments were 10%, 5% and no quartz, respectively, and antigorite with a grain size between $45\text{-}106\ \mu\text{m}$. As expected, sample u865 shows the highest peak of talc where the intensity of the peak at 1050 cm^{-1} is higher than the peak 1000 cm^{-1} for antigorite. U885 also shows a peak for talc but with a lower intensity at reciprocal wavelength 1050 cm^{-1} , the antigorite peak at 1000 cm^{-1} has a higher intensity. The second peak for talc at reciprocal wavelength 670 cm^{-1} is also visible in both the analyses of samples u865 and u885. Though, for sample u885 the intensity is very low. In comparison to the other two analyses u894 only shows the same peaks as antigorite and means no reaction took place. The peak for quartz at wavelength 1100 cm^{-1} is lowest for sample u865 while for experiment u885 the intensity of this peak is very low, this peak is absent for sample u894.

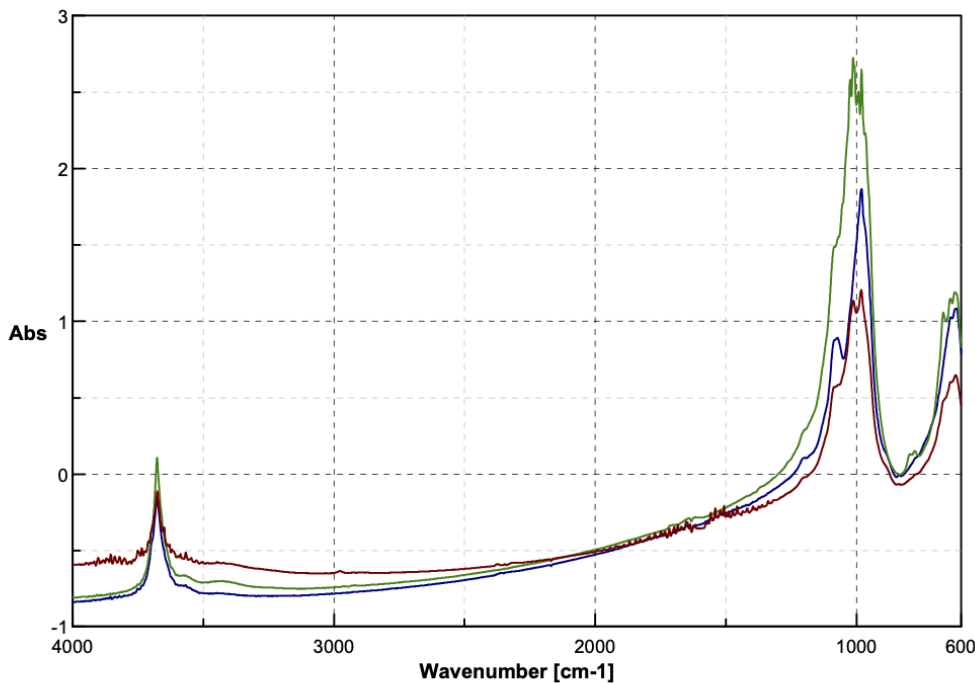


Figure 38: FTIR measurements of three experiments done at 500°C , u865 with 10% quartz (green line), u885 with 5% quartz (red line) and u894 with no quartz (blue line).

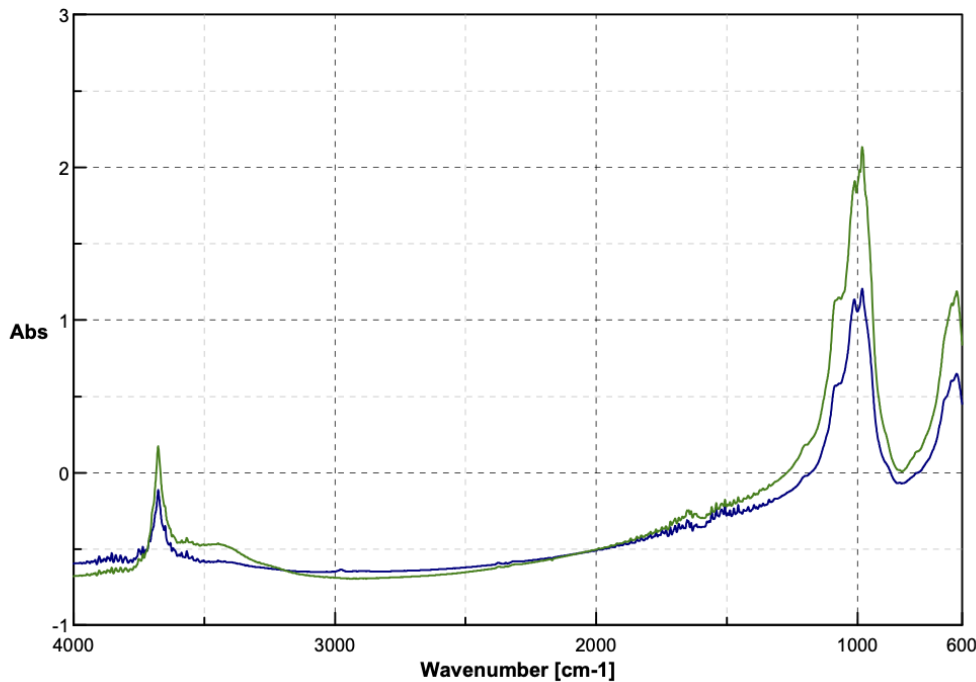


Figure 39: FTIR measurements of two experiments done at 500°C with 5% quartz, u870 with a grain size of 25-45 μm (green line) and u885 with a grain size of 45-106 μm (blue line).

Figure 39 shows experiments u870 and u885 which were both with 5% quartz. However, the two experiments were conducted with antigorite of different grain sizes. U870 was conducted with a grain size of 25-45 μm and experiment u885 with the normal grain size of 45-106 μm . As can be seen in figure 39 experiment u870 shows only a small intensity peak for talc at a wavelength of 1050 cm^{-1} and no peak can be distinguished at 700 cm^{-1} while u885 shows visible talc peaks at both wavelengths.

Figure 40 shows the FTIR measurement of experiment u899 which was conducted at 500°C, 10% quartz and antigorite with a grain size of 25-45 μm . Measurements of u865 and u870 are also shown as reference for talc formation and for comparison between the 5 and 10% quartz for experiments with a grain size of 25-45 μm . experiment u870 shows a peak at both reciprocal wavelengths that belong to talc at 1050 and 700 cm^{-1} . Comparing u899 with u865 shows that at both samples the intensity of the talc peak at 1050 cm^{-1} is higher than the antigorite peak at 1000 cm^{-1} . U870 with 5% quartz has a lower intensity peak at 1050 cm^{-1} as u899.

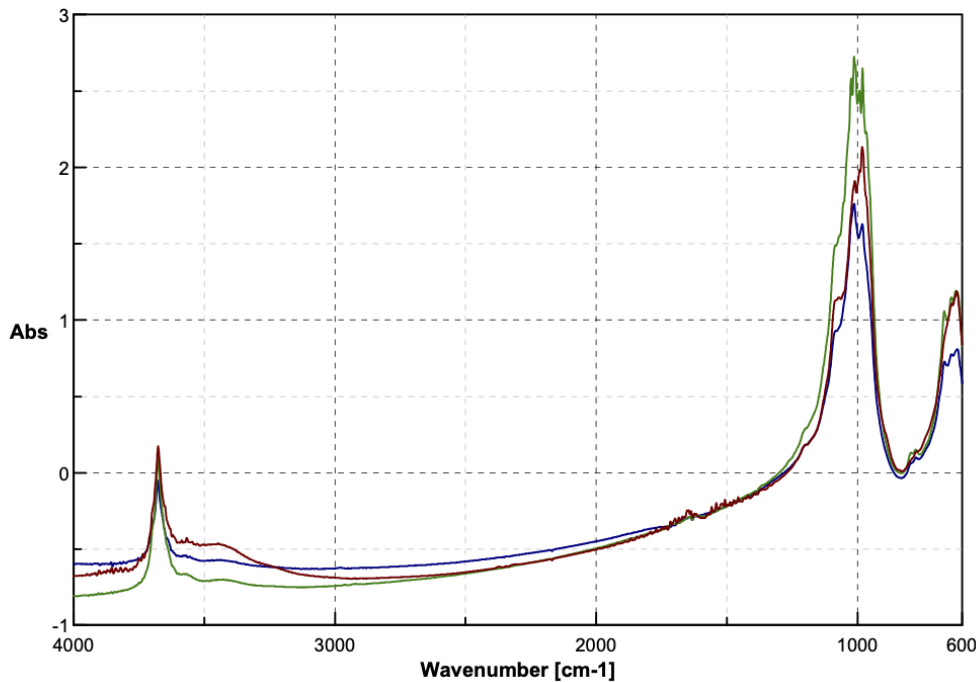


Figure 40: FTIR measurement of experiment u899 (blue line) containing 10% quartz and antigorite with a grain size of 25-45 μm . Experiment u865 (green line) and u870 (red line) are inserted as a reference for the formation of talc.

7 Discussion

7.1 Friction of pure antigorite

I performed experiments on pure antigorite samples at an effective normal stress of 150 MPa, with temperatures ranging from 25 to 500°C and sliding velocities of 0.1 to 100 $\mu\text{m/s}$. The results from the experiments at 25°C show friction coefficients of 0.5 to 0.59, which is comparable with previous work done by Reinen et al. on antigorite gouges at 25°C. They found friction coefficients between 0.5 and 0.85 in bare surface experiments conducted with normal stresses between 25 and 125 MPa and at sliding velocities of 0.01-1 $\mu\text{m/s}$. Other research done on this topic by Okazaki et al. showed that at a velocity of 1.15 $\mu\text{m/s}$, 20°C and 150MPa, friction of a pure antigorite sample was 0.52 which is a small difference from the 0.51 that I measured which could also be due to a different source of antigorite. The (a-b) values of the experiments at 25°C showed a dependence on sliding velocity, with positive values at velocities $<1 \mu\text{m/s}$ and negative values at velocities $>1 \mu\text{m/s}$.

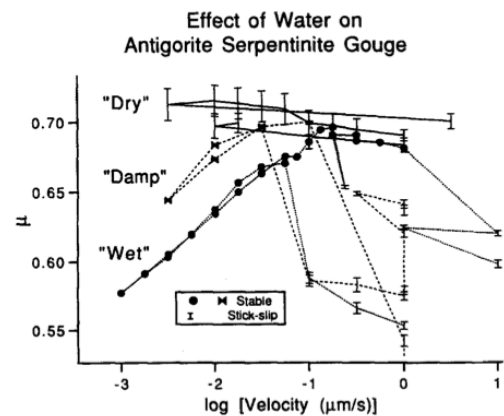


Figure 41: Friction versus velocity. A change from velocity strengthening to weakening happens at 0.05 $\mu\text{m/s}$ (Reinen et al., 1994).

This dependence on velocity has also been noticed by Reinen et al., 1994. They conducted velocity step tests at room temperature where they recorded the steady state friction for the different velocity steps from 0.05 to 1 $\mu\text{m/s}$. They observed a change from velocity strengthening to weakening for their antigorite gouge experiments at 0.1 $\mu\text{m/s}$. D E Moore et al. have also showed this behaviour with their experiments. their experiments done at velocities lower than 1 $\mu\text{m/s}$ there is a velocity weakening effect but their experiments done at velocities faster as 1 $\mu\text{m/s}$ there is a velocity strengthening effect. Reinen et al. proposed that the rate dependence comes from the process of shearing parallel to the layer by dislocation motion, similiar to that which occurs in micas (Kronenberg et al., 1990) which lack Si-O bonds between the adjacent layers. perhaps breaking the Si-O bonds in the antigorite is not rate-dependent because the bonds are spaced far apart in the crystalline structure; and they are broken under the applied stress without much thermal or diffusional assistance (Reinen et al., 1994).

At elevated temperatures friction of pure antigorite is temperature strengthening. and has friction coefficients of 0.5 at 25°C and 0.01 $\mu\text{m/s}$, to 0.78 at 500°C and 100 $\mu\text{m/s}$. Experiments of pure antigorite at 500°C showed stick-slip behaviour and a negative (a-b), while during the fast experiments (a-b) of pure antigorite is only negative at a temperature of 25°C and increases with increasing velocity, Reinen et al. showed that at 25°C (a-b) was negative from a V_1 of 0.03 $\mu\text{m/s}$, which is in comparison with our results. At elevated temperatures, (a-b) is positive with an increase in (a-b) from a velocity of 10 $\mu\text{m/s}$. only at temperatures of 400 and 500 °C a decrease in (a-b) is seen from 30 to 100 $\mu\text{m/s}$.

7.2 Effect of quartz on antigorite

Experiments performed with antigorite mixed with quartz all show a lower friction in comparison with pure antigorite. D E Moore et al. also saw this effect when antigorite was sheared against quartz with a velocity of 0.01 $\mu\text{m/s}$ at 250°C and 100 MPa. Other research from Hirauchi et al. whith a quartz percentage of 30%, at 400°C, a velocity of 0.1 $\mu\text{m/s}$ and 200MPa also shows a drop in friction. All experiments, in my and other research, show a velocity dependence where friction decreases with decreasing velocity. In the conducted experiments the friction coefficient of antigorite mixed with quartz can get as low as 0.216 at 500°C, 150 MPa and a velocity of 0.01 $\mu\text{m/s}$. As D E Moore et al. suggests the low friction can be caused by solution transfer processes caused by the interaction with quartz, which significantly enhances the solubility and/or the rate of dissolution of antigorite. On the other hand, Hirauchi et al. suggest that the low friction is caused by the formation of talc, where the strength of the antigorite decreases toward that of pure talc, when the talc layer thickness approaches one-tenth of the entire hydrous layer thickness. In the next paragraph i will discuss whether these weakening mechanisms were active in my experiments. The microstructural data could explain which weakening mechanism is active. When looking at the sample at 500°C, microprobe analyses confirm the formation of talc in sample u865 which is also validated by EDS and FTIR. The microprobe showed that talc is formed at the grain boundaries of antigorite and the amount decreases grain inward. Talc itself has a friction as low as 0.13 at 150 MPa, 400°C and water saturated (D E Moore et al., 2008). Though, talc might have been present, in the samples at temperatures lower as 500°C, but in too low amount to be detectable by FTIR or because the sample size is only 0.003 gr talc might have not been in that section of the sample. Secondly, the increase of friction after the temperature was dropped to 25°C would be lower or not happen if sufficient talc was formed. moreover, friction would keep decreasing if more talc forms. Though, all experiments at low velocities get to steady state friction. These contradictions suggests that perhaps not enough

talc was formed and another weakening mechanism might be active, such as pressure solution.

EDS and microscopy pictures show a difference in deformation between the two grain sizes used and between the 5 and 10% quartz at 500°C. When 5% quartz is added to antigorite with a grain size of 45-106 μm , deformation is localized, while a quartz percentage of 10% causes deformation distributed throughout the sample. Antigorite with a grain size between 25 and 45 μm and 5% quartz shows localized deformation in the localized slip zone. When comparing microscopy pictures of samples where quartz was added with samples of only antigorite the samples containing quartz undergo grain reduction to a greater extent. One of the reasons for grain reduction can be due to the presence of quartz and its effect on the solubility of antigorite. The dissolution of quartz changes the pH of the solution which enhances the solubility of antigorite. If antigorite is more soluble grains are more easily broken down.

Chester et al. and Kanagawa et al. suggested that solution transport may be activated in the presence of quartz gouge in a fault at hydrothermal conditions. To assess this suggestion equation 7, from chapter 2.3, was used to calculate the activation energy. The activation energy for dissolution controlled processes lies within 14 and 20 KJ/mol. Using equation 7 on the measured results from my experiments gives an activation energy of 4.254 KJ/mol. This value is too low for dissolution controlled processes. Though when friction is compensated with the friction

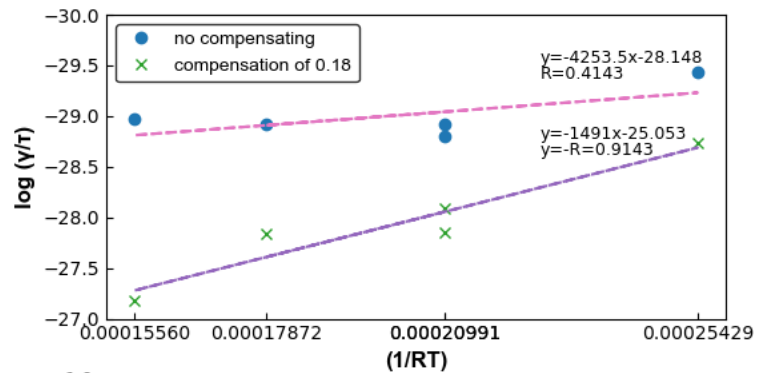


Figure 42: Log (γ/τ) versus $1/RT$ with and without compensation of talc. The trendline shows the activation energy and the R values which were used to find the best fit.

coefficient of talc the activation energy is 14.291 KJ/mol, see figure 42. Compensation is done by subtracting the friction of talc from the measured friction. Using trial and error a best fit model was found using a friction coefficient for talc of 0.18, using this friction the trend-line had the highest R value. This friction was used for every temperature. Because the activation energy, when compensated for talc, falls within the range of activation energy for dissolution controlled processes, this suggests that both processes are active during shearing.

Incongruent pressure solution might also be the case for the low fault strength and aseismic behaviour, even when low amount of talc are formed. This means that pressure solution would be the main weakening mechanism and that the talc formation is a result of the incongruent pressure solution.

7.3 Effect of quartz on (a-b)

The (a-b) results show that antigorite at most temperatures and velocities has a positive (a-b) which means conditionally stable fault movement. Though, in all experiments a drop in (a-b) occurs around 300°C. The drop in (a-b) suggests that the velocity dependence of frictional strength of antigorite is temperature sensitive. One explanation for this drop is the formation of talc. Though, Diane E Moore et al. showed that antigorite mixed with different percentages of talc at 400°C, 100

MPa and a V_1 of $0.1 \mu\text{m/s}$, give negative (a-b) values at talc percentages less than 50%. Looking at the microstructural analyses this amount of talc is not formed during my experiments. Another observation is that at high temperatures (a-b) gets lower with increasing velocity while at low temperatures (a-b) increases with increasing velocity.

Masuda et al. showed that quartz also shows the lowest (a-b) value at a temperature of 300°C (see figure 43). For quartz this change in (a-b) is induced through a change in deformation mechanism. Up to $300\text{-}350^\circ\text{C}$, quartz deforms by brittle mechanisms. At higher temperatures, crystal plastic mechanisms and diffusion dominate. Due to the wet conditions of their experiments they also suggest that pressure solution is active.

Quartz also shows a velocity dependence with increasing temperature. Chester et al. have verified through microstructural analyses that the velocity dependence in quartzite with increasing temperature is correlated to a change in deformation mechanism. Under wet conditions solution-precipitation processes dominate. Decreasing velocity increases the time of contact of asperities on the sliding surfaces, allowing more time for deformation to occur.

Masuda et al. also added quartz to a plagioclase-pyroxene mixture and noticed that when quartz was added friction went from velocity weakening to velocity strengthening. Looking at these results, their suggestions and evidence for a change in deformation mechanism it might also be true for antigorite. The decrease in (a-b) up to 300°C is mostly by grain size reduction, due to the enhanced solubility of antigorite by the presence of quartz, and at higher temperatures by pressure solution and talc formation.

The amount of quartz added to antigorite can change the temperature at which the drop in (a-b) happens. This could suggest that quartz changes the velocity dependence of friction of antigorite. Alternately, that the formation of talc, due to the presence of quartz, changes the velocity dependence.

7.4 Comments on reproducibility of final friction

The experiments with an antigorite/ quartz mixture gave an insight in the material properties at different conditions and compositions. For experiments u865 and u888, conducted under identical conditions, a difference of 0.022 in steady state friction was measured. This difference can be explained by several reasons. The first explanation is the time an experiment was ran. If an experiment's duration was longer deformation mechanisms like pressure solution would have more time to be active which could increase talc production or could lead to further grain size reduction, which in return decreases friction. This explanation is supported by D E Moore et al. They found that friction of their 75% pure antigorite sample was higher at velocities lower than $1 \mu\text{m/s}$ than at velocities faster than $1 \mu\text{m/s}$. They suggested an operation of a time-dependent strengthening

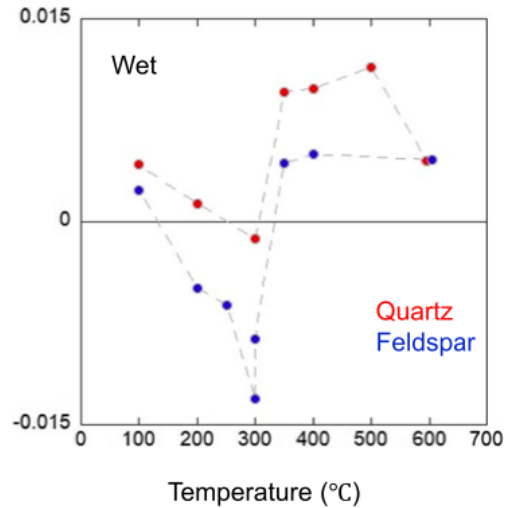


Figure 43: (a-b) versus temperature (Masuda et al., 2019).

process that is independent of the changes in μ associated with the velocity step. A second explanation is the composition of the starting material. The antigorite needed to be crushed twice to get a sufficient amount of 45-106 μm antigorite which means that the second time the grain size distribution might have been different from the first time. If the distribution was shifted more to 45 μm or the other way around more towards 106 μm it could change the friction development because of the grain size dependence shown during my research.

The experiments conducted at 25 and 200°C at slow velocities show small increase in friction when velocity is stepped down from 1 to 0.01 $\mu\text{m/s}$, before friction decreases again. At higher temperatures the friction decreases immediately after the velocity downstep and the friction decrease is faster at higher temperatures. This means that friction of a mixture with 90% antigorite and 10% quartz is time and temperature dependent which is an additional indication for the operation of a time-dependent mechanism such as pressure solution.

Lower friction is also reached when smaller grain sizes are used. This difference in friction development between the two grain sizes could be due to several reasons. One reason is that due to a smaller grain size, and thus extended grain boundaries, quartz is better distributed throughout the sample and the antigorite can react faster into talc which decreases friction. Though, FTIR and EDS do not show sufficient talc formation. Further does friction increase again when the temperature is dropped from 500 to 25°C. If sufficient talc was formed this increase would not have happened or would be less. The second one is again pressure solution. This can happen faster with a smaller grain size due to a faster diffusion pathway.

In this research the friction differs between the experiments where 5 or 10% quartz was added. Comparing this with the research of Hirauchi et al. who used 70% antigorite and 30% quartz at °C give approximately the same steady state friction coefficient as my experiments with 10% quartz. This would suggest that after a certain percentage of quartz friction is not lowered anymore.

7.5 Implications for nature

The results of the experiments of pure antigorite indicate that antigorite alone can not be the cause of creep within subduction zones and the San Andreas fault. But, adding quartz to antigorite decreases the friction substantially and in the lab causes aseismic behaviour. In subduction zones this means that the addition of siliceous fluid coming from the subducting crust can infiltrate the hydrated forearc mantle wedge and form talc to a certain degree. In subduction zones talc has been reported in exhumed thrust faults (Simon M Peacock, 1987; King et al., 2003). Within the San Andreas fault, silica content from heated ground water and from metastably deposited quartz veins can form talc. Within the San Andreas fault, talc is found in borehole rocks from the San Andreas Fault Observatory at Depth (SAFOD) (Gratier et al., 2011). Moreover, the silicon within subduction zones and the San Andreas fault will activate solution transfer processes and pressure solution will decrease friction even more which can cause aseismic behaviour.

Incongruent pressure solution observed in the experiments might also explain the low fault strength as well as the aseismic behaviour. In this scenario, pressure solution is the main weakening mechanism and as a result of incongruent pressure solution small amounts of talc are formed.

8 Conclusion

The aim of this research was to study the effect of quartz on the friction of antigorite, which is an important mineral involved in the subduction zone interface in the forearc mantle wedge as well as in the San Andreas fault. Antigorite was sheared in the rotary shear apparatus at various temperatures and velocities mixed with 0, 5 or 10% quartz. The results may give a clue into the fault strength and aseismic behaviour of the subduction zone interface in hydrated forearc mantle wedges and the San Andreas fault.

- pure antigorite shows stick-slip behaviour and can not solely explain the aseismic behaviour seen in subduction zones and the San Andreas fault

- Antigorite with a quartz percentage of 10% is temperature weakening and only at 25°C does it show velocity strengthening. Which may be because quartz has little to no effect at lower temperatures. From a temperature of 100°C the friction development is velocity weakening and shows aseismic behaviour. Which may be due to talc formation and pressure solution being active from this temperature.

- The amount of quartz and thus siliceous fluid or quartz veins within fault zones has a significant effect on the production of talc and pressure solution within antigorite gouges. This may be due to the effect quartz has on the solubility of antigorite.

- Grain size is an important determinant for the friction decrease within antigorite. The smaller the grain size the lower the friction. This may be because pressure solution happens faster when the surface area is bigger.

- At 300°C there is a significant drop in the (a-b) value. The temperature at which this drop happens changes with different amounts of quartz. And because for quartz this is explained by a change in deformation mechanism this needs more research as it might be important in explaining the aseismic behaviour at temperatures higher as 350°C.

To conclude, the siliceous fluid from the subducting slab infiltrating the hydrated forearc mantle wedge and the siliceous fluid and quartz veins in the San Andreas fault, produce talc which lowers the friction. The amount of silica within the fluid determines how much talc will be formed. Though, this is not the only active deform mechanism. Pressure solution is also active and likewise will lower friction. This lowering from both the talc and pressure solution can be the cause of the aseismic behaviour seen in forearc mantle wedges and the San Andreas fault.

9 Acknowledgements

I would like to thank Andre Niemeijer and Ake Fagerang for guiding me throughout my thesis and helping me during my experimental phase. Furthermore i would like to thank Erik Hellebrand for getting my microprobe results, Maartje Hamers for making the EDS analyses, Oliver Plömpfer for letting me use his antigorite during the experiments and lastly the EPOS-MINT facility.

References

Allen, L J et al. (2012). "Chemical mapping at atomic resolution using energy-dispersive x-ray spectroscopy". In: *MRS bulletin* 37.1, pp. 47–52.

- Angiboust, S et al. (2012). "Effect of fluid circulation on subduction interface tectonic processes: Insights from thermo-mechanical numerical modelling". In: *Earth and Planetary Science Letters* 357, pp. 238–248.
- Audet, P and R Bürgmann (2014). "Possible control of subduction zone slow-earthquake periodicity by silica enrichment". In: *Nature* 510.7505, pp. 389–392.
- Bach, W et al. (2004). "Seawater-peridotite interactions: First insights from ODP Leg 209, MAR 15 N". In: *Geochemistry, Geophysics, Geosystems* 5.9.
- Bebout, G E and M D Barton (1989). "Fluid flow and metasomatism in a subduction zone hydrothermal system: Catalina Schist terrane, California". In: *Geology* 17.11, pp. 976–980.
- Bos, B and C J Spiers (2002). "Frictional-viscous flow of phyllosilicate-bearing fault rock: Microphysical model and implications for crustal strength profiles". In: *Journal of Geophysical Research: Solid Earth* 107.B2, ECV–1.
- Boschi, C, G L Fruh-Green, and J Escartin (2006). "Occurrence and significance of serpentinite-hosted, talc-and amphibole-rich fault rocks in modern oceanic settings and ophiolite complexes: An overview". In: *Ophioliti* 31.2, pp. 129–140.
- Brace, WF and JD Byerlee (1966). "Stick-slip as a mechanism for earthquakes". In: *Science* 153.3739, pp. 990–992.
- Büttner, Steffen H (2012). "Rock Maker: an MS Excel™ spreadsheet for the calculation of rock compositions from proportional whole rock analyses, mineral compositions, and modal abundance". In: *Mineralogy and Petrology* 104.1, pp. 129–135.
- Carmignano, O R DR et al. (2020). "Serpentinites: mineral structure, properties and technological applications". In: *Journal of the Brazilian Chemical Society* 31.1, pp. 2–14.
- Chester, FM and NG Higgs (1992). "Multimechanism friction constitutive model for ultrafine quartz gouge at hypocentral conditions". In: *Journal of Geophysical Research: Solid Earth* 97.B2, pp. 1859–1870.
- d'Alfonso, AJ et al. (2010). "Atomic-resolution chemical mapping using energy-dispersive x-ray spectroscopy". In: *Physical Review B* 81.10, p. 100101.
- Den Hartog, S, AR Niemeijer, and C J Spiers (2012). "New constraints on megathrust slip stability under subduction zone P–T conditions". In: *Earth and Planetary Science Letters* 353, pp. 240–252.
- Evans, BW, EVANS BW, et al. (1976). "stability of chrysotile and antigorite in the serpentinite multsystem." In:
- French, M E, G Hirth, and K Okazaki (2019). "Fracture-induced pore fluid pressure weakening and dehydration of serpentinite". In: *Tectonophysics* 767, p. 228168.
- Gratier, J-P et al. (2011). "Aseismic sliding of active faults by pressure solution creep: Evidence from the San Andreas Fault Observatory at Depth". In: *Geology* 39.12, pp. 1131–1134.
- Hilaret, N and B Reynard (2009). "Stability and dynamics of serpentinite layer in subduction zone". In: *Tectonophysics* 465.1-4, pp. 24–29.
- Hirauchi, K, S AM den Hartog, and C J Spiers (2013). "Weakening of the slab–mantle wedge interface induced by metasomatic growth of talc". In: *Geology* 41.1, pp. 75–78.
- Holland, TJB and RTJB Powell (1998). "An internally consistent thermodynamic data set for phases of petrological interest". In: *Journal of metamorphic Geology* 16.3, pp. 309–343.
- Hsu, C-P Sherman et al. (1997). "Infrared spectroscopy". In: *Handbook of instrumental techniques for analytical chemistry* 247, p. 277.
- Hyndman, D and Simon M Peacock (2003). "Serpentinization of the forearc mantle". In: *Earth and Planetary Science Letters* 212.3-4, pp. 417–432.

- Hyndman, R D and K Wang (1993). "Thermal constraints on the zone of major thrust earthquake failure: The Cascadia subduction zone". In: *Journal of Geophysical Research: Solid Earth* 98.B2, pp. 2039–2060.
- Irving, AJ, W-L Huang, and PJ Wyllie (1977). "Phase relations of portlandite, $\text{Ca}(\text{OH})_2$ and brucite, $\text{Mg}(\text{OH})_2$ to 33 kilobars". In: *American Journal of Science* 277.3, pp. 313–321.
- Kanagawa, K, S F Cox, and S Zhang (2000). "Effects of dissolution-precipitation processes on the strength and mechanical behavior of quartz gouge at high-temperature hydrothermal conditions". In: *Journal of Geophysical Research: Solid Earth* 105.B5, pp. 11115–11126.
- King, Robert L, Matthew J Kohn, and John M Eiler (2003). "Constraints on the petrologic structure of the subduction zone slab-mantle interface from Franciscan Complex exotic ultramafic blocks". In: *GSA Bulletin* 115.9, pp. 1097–1109.
- Kirby, S H (1983). "Rheology of the lithosphere". In: *Reviews of Geophysics* 21.6, pp. 1458–1487.
- Kronenberg, A K, S H Kirby, and J Pinkston (1990). "Basal slip and mechanical anisotropy of biotite". In: *Journal of Geophysical Research: Solid Earth* 95.B12, pp. 19257–19278.
- Logan, JM et al. (1992). "Fabrics of experimental fault zones: Their development and relationship to mechanical behavior". In: *International geophysics*. Vol. 51. Elsevier, pp. 33–67.
- Manning, C E (1995). "Phase-equilibrium controls on SiO_2 metasomatism by aqueous fluid in subduction zones: reaction at constant pressure and temperature". In: *International Geology Review* 37.12, pp. 1074–1093.
- (1996). "Effect of sediments on aqueous silica transport in subduction zones". In: *Washington DC American Geophysical Union Geophysical Monograph Series* 96, pp. 277–284.
- Marone, C (1998). "Laboratory-derived friction laws and their application to seismic faulting". In: *Annual Review of Earth and Planetary Sciences* 26.1, pp. 643–696.
- Masuda, K, T Arai, and M Takahashi (2019). "Effects of frictional properties of quartz and feldspar in the crust on the depth extent of the seismogenic zone". In: *Progress in Earth and Planetary Science* 6.1, pp. 1–8.
- Moore, D E and D A Lockner (2008). "Talc friction in the temperature range 25–400 C: Relevance for fault-zone weakening". In: *Tectonophysics* 449.1-4, pp. 120–132.
- (2013). "Chemical controls on fault behavior: Weakening of serpentinite sheared against quartz-bearing rocks and its significance for fault creep in the San Andreas system". In: *Journal of Geophysical Research: Solid Earth* 118.5, pp. 2558–2570.
- Moore, D E et al. (1997). "Strengths of serpentinite gouges at elevated temperatures". In: *Journal of Geophysical Research: Solid Earth* 102.B7, pp. 14787–14801.
- Moore, Diane E and David A Lockner (2011). "Frictional strengths of talc-serpentine and talc-quartz mixtures". In: *Journal of Geophysical Research: Solid Earth* 116.B1.
- Moore, E and J Rymer (2007). "Talc-bearing serpentinite and the creeping section of the San Andreas fault". In: *Nature* 448.7155, pp. 795–797.
- Niemeijer, A et al. (2020). "Faulting in the laboratory". In: *Understanding Faults*. Elsevier, pp. 167–220.
- Niemeijer, AR, CJ Spiers, and CJ Peach (2008). "Frictional behaviour of simulated quartz fault gouges under hydrothermal conditions: Results from ultra-high strain rotary shear experiments". In: *Tectonophysics* 460.1-4, pp. 288–303.
- Okazaki, K, I Katayama, and M Takahashi (2013). "Effect of pore fluid pressure on the frictional strength of antigorite serpentinite". In: *Tectonophysics* 583, pp. 49–53.
- Padrón-Navarta, J A et al. (2013). "Tschermak's substitution in antigorite and consequences for phase relations and water liberation in high-grade serpentinites". In: *Lithos* 178, pp. 186–196.

- Passchier, C W and R AJ Trouw (2005). *Microtectonics*. Springer Science & Business Media.
- Peacock, S M and R D Hyndman (1999). "Hydrous minerals in the mantle wedge and the maximum depth of subduction thrust earthquakes". In: *Geophysical Research Letters* 26.16, pp. 2517–2520.
- Peacock, Simon M (1987). "Serpentinization and infiltration metasomatism in the Trinity peridotite, Klamath province, northern California: implications for subduction zones". In: *Contributions to Mineralogy and Petrology* 95.1, pp. 55–70.
- Perrillat, J et al. (2005). "Kinetics of antigorite dehydration: a real-time X-ray diffraction study". In: *Earth and Planetary Science Letters* 236.3-4, pp. 899–913.
- product data: silica ground (n.d.). Brenntag Specialties, inc.
- Reinen, L A, J D Weeks, and T E Tullis (1994). "The frictional behavior of lizardite and antigorite serpentinites: Experiments, constitutive models, and implications for natural faults". In: *Pure and Applied Geophysics* 143.1, pp. 317–358.
- Reynard, B (2013). "Serpentine in active subduction zones". In: *Lithos* 178, pp. 171–185.
- Rutter, EH (1983). "Pressure solution in nature, theory and experiment". In: *Journal of the Geological Society* 140.5, pp. 725–740.
- Shindo, D and T Oikawa (2002). "Energy dispersive x-ray spectroscopy". In: *Analytical electron microscopy for materials science*. Springer, pp. 81–102.
- Technology Zurich, Swiss Federal Institute of (n.d.). *Perple_x*. <https://www.perplex.ethz.ch>.
- Ulmer, P and V Trommsdorff (1995). "Serpentine stability to mantle depths and subduction-related magmatism". In: *Science* 268.5212, pp. 858–861.
- Verberne, B A et al. (2015). "Mechanical behavior and microstructure of simulated calcite fault gouge sheared at 20–600 C: Implications for natural faults in limestones". In: *Journal of Geophysical Research: Solid Earth* 120.12, pp. 8169–8196.
- Wunder, B and W Schreyer (1997). "Antigorite: High-pressure stability in the system MgO SiO₂ H₂O (MSH)". In: *Lithos* 41.1-3, pp. 213–227.

10 Appendices

10.1 Appendix 1

Friction versus $\log(\text{velocity})$ for experiments u875, u877 and u883 at the different temperatures. These graphs give an extra insight in the velocity weakening behaviour at room temperature.

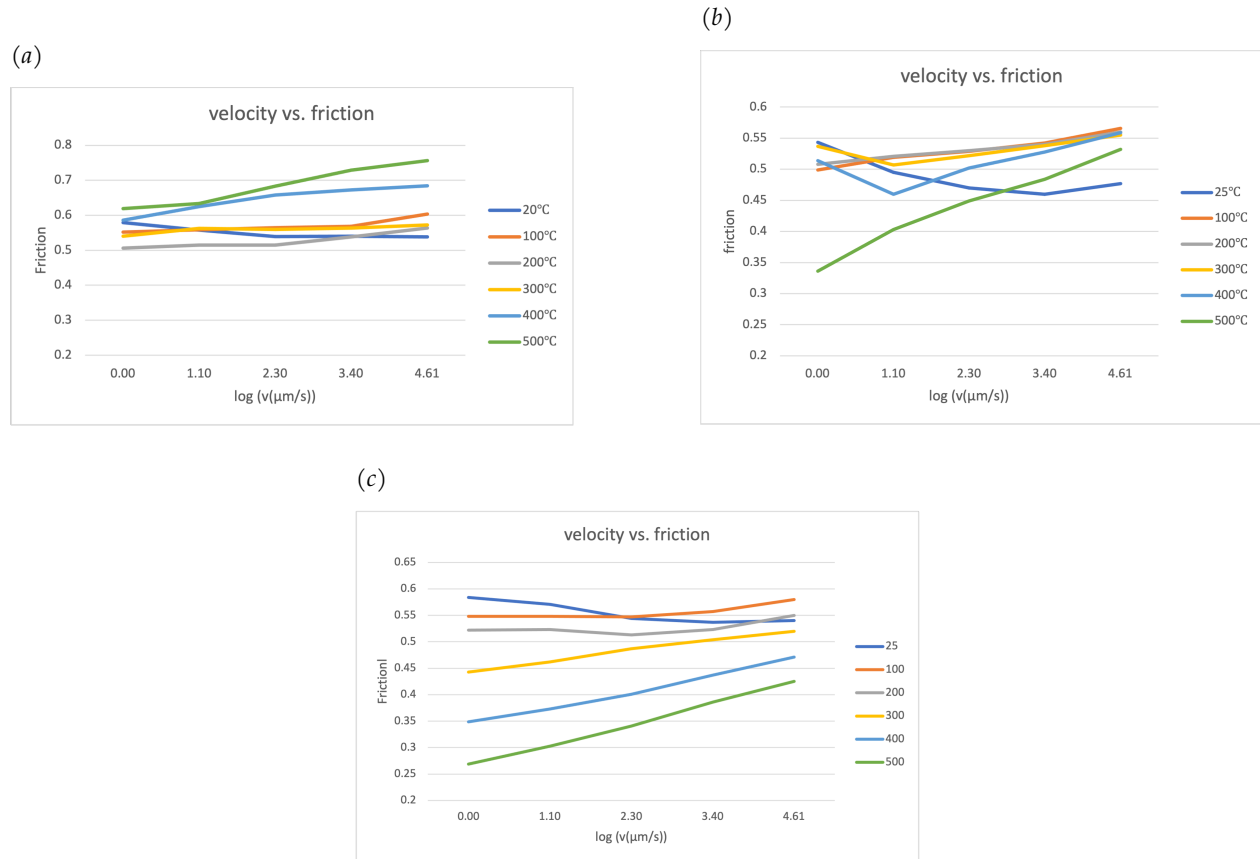


Figure 44: the graphs show the velocity against friction for the experiments where temperature and velocity were changed. A) shows the results of friction for the experiments where no quartz was added. This graph shows the temperature strengthening of antigorite. B) This graph shows the friction of the experiment where 5% quartz was added. It shows a decrease in friction at higher temperatures. C) shows the results of friction for the experiment where 10% quartz was added. The decrease in friction is even lower and at a lower temperature.

10.2 Appendix 2

Results taken from previous research and the conditions they were conducted at.

composition	normal stress(MPa)	temperature (°C)	velocity ($\mu\text{m/s}$)	steady state friction
Hirauchi et. Al (2013)				
70%atg + 30% qtz	200	400	30	0,45
70%atg + 30% qtz	200	400	3,7	0,36
70%atg + 30% qtz	200	400	0,3	0,32
70%atg + 30% qtz	200	400	0,1	0,26
70%atg + 30% qtz	200	400	3,5	0,55 and rising
Moore & Lockner (2013)				
antigorite only	100	250	0,0115	0,56 and decreasing
antigorite between granite	100	250	0,01	0,35
antigorite between quartz	100	250	0,1	0,49 doesn't meet steady state
antigorite between quartz	100	250	0,01	0,35 close to steady state
Moore & Lockner (1997)				
75% pure atg	100	25	0,1-0,32-1	All temp. strain hardening. velocity strengthening. and a higher temperature means lower friction.
75% pure atg	100	97	0,1-0,32-1	
75% pure atg	100	194	0,1-0,32-1	
75% pure atg	100	25 & 97	>1	At higher velocity friction is lower than <1 velocity
75% pure atg	100	194	>1	At higher velocity friction is higher than <1 velocity
Okazaki (2013)				
98% pure atg	150	20	1,15	0,52

Table 4: results and conditions from previous research

10.3 Appendix 3

Results of the microprobe analyses for sample u865.

SAMPLE	SiO2	TiO2	Al2O3	Cr2O3	FeO	MnO	MgO	CaO	NiO	Na2O	K2O	Cl	O	H2O	TOTAL
u865-bottom-test_serp	42.85	0.02	1.58	0.00	4.52	0.07	37.51	0.02	0.13	0.00	0.01	0.00	0.00	12.78	99.50
u865-top_img3_serp-left_H:O=0.44	45.43	0.02	1.45	0.00	4.13	0.06	35.99	0.02	0.13	0.00	0.01	0.00	0.00	12.88	100.12
u865-top_img3_serp-left_H:O=0.44	44.37	0.00	1.51	0.00	4.25	0.08	36.54	0.03	0.15	0.00	0.01	0.00	0.00	12.84	99.78
u865-top_img3_serp-left_H:O=0.44	45.38	0.01	1.40	0.00	4.18	0.09	35.93	0.04	0.12	0.02	0.02	0.00	0.00	12.87	100.06
u865-top_img3_pore-under-qtz_H:O=0.1	71.00	0.00	0.87	0.01	2.52	0.05	22.97	0.02	0.07	0.03	0.02	0.00	0.00	2.83	100.38
u865-top_img3_serp-under-pore_H:O=0.3	49.95	0.00	1.48	0.00	4.25	0.09	35.31	0.04	0.13	0.01	0.02	0.00	0.00	8.44	99.72
u865-top_img3_pore-bottom-left-corner_H:O=0.2	56.33	0.00	1.06	0.00	3.54	0.07	32.47	0.06	0.09	0.04	0.02	0.00	0.00	5.58	99.28
u865-top_img5_serp-left_H:O=0.44	45.05	0.01	1.46	0.00	4.15	0.09	37.18	0.03	0.14	0.00	0.02	0.00	0.00	12.83	100.97
u865-top_img5_serp-left_H:O=0.44	44.85	0.00	1.59	0.00	4.14	0.10	37.20	0.05	0.14	0.00	0.02	0.01	0.00	12.83	100.92
u865-top_img5_serp-left_H:O=0.44	45.03	0.01	1.57	0.01	4.07	0.09	36.52	0.03	0.16	0.00	0.02	0.00	0.00	12.86	100.36
u865-top_img5_serp-left_H:O=0.44	45.67	0.00	1.65	0.00	4.22	0.10	36.58	0.05	0.15	0.02	0.01	0.00	0.00	12.84	101.29
u865-top_img5_bright-interstitial1_H:O=0.2	54.27	0.00	1.13	0.01	3.56	0.09	34.68	0.03	0.13	0.03	0.02	0.00	0.00	5.54	99.49
u865-top_img5_bright-interstitial2_H:O=0.25	54.14	0.01	1.24	0.01	3.73	0.07	33.00	0.04	0.18	0.04	0.03	0.00	0.00	7.03	99.51
u865-top_img5_bright-interstitial3_H:O=0.25	53.75	0.00	1.39	0.01	3.91	0.08	33.15	0.04	0.19	0.05	0.03	0.01	0.00	7.01	99.63
u865-top_img5_serp-rim1_H:O=0.3	51.52	0.02	1.04	0.00	3.71	0.08	34.28	0.03	0.15	0.01	0.02	0.02	0.00	8.50	99.37
u865-top_img5_serp-rim2_H:O=0.35	47.27	0.00	1.41	0.00	4.11	0.09	37.64	0.05	0.13	0.02	0.02	0.00	0.00	9.90	100.64
u865-top_img5_serp-rim3_H:O=0.3	48.50	0.00	1.38	0.00	4.06	0.08	37.74	0.05	0.15	0.02	0.02	0.00	0.00	8.39	100.40
u865-top_img5_serp-rim4_H:O=0.25	49.50	0.00	1.52	0.00	4.01	0.08	37.78	0.05	0.14	0.01	0.01	0.00	0.00	6.92	100.02
u865-top_img5_serp-rim5_H:O=0.25	51.77	0.01	1.59	0.01	4.01	0.10	35.65	0.04	0.12	0.02	0.02	0.01	0.00	6.96	100.30
u865-top_img4_shearzone-bright_H:O=0.3	50.07	0.02	1.42	0.00	3.95	0.07	35.69	0.04	0.12	0.03	0.03	0.01	0.00	8.45	99.88
u865-top_img4_shearzone-dark_H:O=0.4	48.19	0.00	1.50	0.00	4.27	0.06	35.24	0.04	0.15	0.01	0.02	0.00	0.00	10.88	100.35

Figure 45: Composition of oxides in sample u865. Measured with the microprobe.

10.4 Appendix 4

Results of the microprobe for sample u866. The values on this sheet were used for the results in table 1.

SAMPLE	SiO2	TiO2	Al2O3	Cr2O3	FeO	MnO	MgO	CaO	NiO	Na2O	K2O	Cl	O	H2O	TOTAL
u866-fragment1 (all serpentines, with H:O=0.444)	43.27	0.01	1.50	0.01	4.36	0.06	37.37	0.01	0.17	0.00	0.01	0.01	0.00	12.80	99.57
u866-fragment1	43.44	0.00	1.54	0.01	4.43	0.10	38.28	0.03	0.15	0.01	0.01	0.00	0.00	12.76	100.76
u866-fragment1	42.54	0.00	1.50	0.00	4.36	0.08	36.14	0.03	0.15	0.01	0.01	0.01	0.00	12.83	97.67
u866-fragment2	43.45	0.01	1.45	0.00	4.27	0.10	38.27	0.02	0.18	0.01	0.01	0.01	0.00	12.77	100.55
u866-fragment2	43.75	0.01	1.37	0.00	4.28	0.08	37.49	0.01	0.14	0.00	0.01	0.01	0.00	12.81	99.95
u866-fragment2	42.56	0.00	1.32	0.00	4.25	0.10	36.03	0.03	0.13	0.00	0.01	0.01	0.00	12.85	97.28
u866-fragment3	43.51	0.01	1.54	0.00	4.20	0.09	36.70	0.02	0.14	0.00	0.01	0.00	0.00	12.84	99.05
u866-fragment3	43.77	0.00	1.50	0.00	4.22	0.09	37.64	0.03	0.14	0.00	0.00	0.00	0.00	12.80	100.20
u866-fragment3	43.36	0.00	1.44	0.00	4.21	0.09	36.62	0.02	0.12	0.00	0.01	0.01	0.00	12.84	98.73
u866-fragment4	42.26	0.01	1.56	0.01	4.42	0.09	37.53	0.02	0.15	0.00	0.01	0.01	0.00	12.78	98.86
u866-fragment4	43.21	0.00	1.50	0.00	4.50	0.11	37.33	0.02	0.16	0.00	0.01	0.01	0.00	12.79	99.62
u866-fragment4	42.27	0.01	1.39	0.00	4.37	0.07	34.91	0.02	0.17	0.00	0.01	0.01	0.00	12.87	96.10
u866-fragment5	42.86	0.00	1.48	0.01	4.32	0.07	37.53	0.02	0.14	0.02	0.01	0.00	0.00	12.80	99.26
u866-fragment5	42.83	0.02	1.51	0.00	4.26	0.07	38.15	0.01	0.13	0.00	0.01	0.01	0.00	12.78	99.79
u866-fragment5	42.63	0.00	1.52	0.00	4.29	0.08	38.33	0.01	0.14	0.00	0.01	0.01	0.00	12.77	99.79
u866-fragment6	42.54	0.00	1.45	0.02	4.28	0.12	37.53	0.02	0.13	0.00	0.02	0.00	0.00	12.79	98.91
u866-fragment6	43.80	0.01	1.57	0.01	4.45	0.10	38.46	0.01	0.47	0.00	0.01	0.00	0.00	12.73	101.64
u866-fragment6	43.77	0.02	1.64	0.01	4.26	0.07	36.82	0.01	0.11	0.00	0.01	0.01	0.00	12.83	99.57
u866-fragment7	42.48	0.01	1.49	0.00	4.03	0.10	36.83	0.02	0.17	0.00	0.01	0.01	0.00	12.83	97.99
u866-fragment7	42.97	0.00	1.39	0.00	4.22	0.11	35.89	0.03	0.16	0.00	0.01	0.01	0.00	12.85	97.64
u866-fragment7	43.13	0.00	1.43	0.00	4.11	0.14	36.66	0.02	0.15	0.00	0.01	0.00	0.00	12.84	98.49
u866-fragment8	43.61	0.01	1.40	0.00	4.37	0.07	37.43	0.01	0.16	0.00	0.00	0.00	0.00	12.80	99.87
u866-fragment8	43.59	0.00	1.43	0.00	4.50	0.10	37.91	0.01	0.15	0.00	0.02	0.00	0.00	12.77	100.47
u866-fragment8	42.65	0.01	1.57	0.00	4.47	0.09	37.84	0.01	0.15	0.00	0.01	0.01	0.00	12.77	99.58
u866-fragment9	44.03	0.00	1.40	0.01	4.34	0.08	38.12	0.01	0.13	0.00	0.01	0.00	0.00	12.78	100.93
u866-fragment9	43.53	0.01	1.37	0.01	4.23	0.10	37.71	0.01	0.11	0.01	0.01	0.01	0.00	12.80	99.91
u866-fragment9	44.01	0.01	1.45	0.00	4.45	0.08	37.20	0.03	0.12	0.01	0.01	0.00	0.00	12.80	100.19
u866-fragment10	43.05	0.00	1.42	0.00	4.17	0.09	36.96	0.03	0.16	0.00	0.00	0.01	0.00	12.83	98.72
u866-fragment10	43.52	0.01	1.47	0.00	4.35	0.09	36.76	0.02	0.17	0.01	0.01	0.00	0.00	12.82	99.22
u866-fragment10	43.04	0.00	1.41	0.00	4.24	0.09	36.70	0.03	0.15	0.00	0.02	0.01	0.00	12.83	98.52
u866-fragment11	43.68	0.01	1.40	0.00	4.34	0.09	38.07	0.01	0.15	0.01	0.01	0.00	0.00	12.78	100.55
u866-fragment11	43.21	0.00	1.39	0.00	4.32	0.11	37.73	0.01	0.12	0.00	0.02	0.00	0.00	12.79	99.69
u866-fragment11	42.63	0.00	1.39	0.00	4.17	0.08	37.66	0.01	0.13	0.00	0.01	0.00	0.00	12.81	98.89

Figure 46: Composition of oxides in sample u866. measured with the microprobe.